Second order symmetry-preserving conservative Lagrangian scheme for compressible Euler equations in two-dimensional cylindrical coordinates

Juan Cheng[1] and Chi-Wang Shu[2]

Abstract

In applications such as astrophysics and inertial confinement fusion, there are many three-dimensional cylindrical-symmetric multi-material problems which are usually simulated by Lagrangian schemes in the two-dimensional cylindrical coordinates. For this type of simulation, a critical issue for the schemes is to keep spherical symmetry in the cylindrical coordinate system if the original physical problem has this symmetry. In the past decades, several Lagrangian schemes with such symmetry property have been developed, but all of them are only first order accurate. In this paper, we develop a second order cell-centered Lagrangian scheme for solving compressible Euler equations in cylindrical coordinates, based on the control volume discretizations, which is designed to have uniformly second order accuracy and capability to preserve one-dimensional spherical symmetry in a two-dimensional cylindrical geometry when computed on an equal-angle-zoned initial grid. The scheme maintains several good properties such as conservation for mass, momentum and total energy, and the geometric conservation law. Several two-dimensional numerical examples in cylindrical coordinates are presented to demonstrate the good performance of the scheme in terms of accuracy, symmetry, non-oscillation and robustness. The advantage of higher order accuracy is demonstrated in these examples.

Keywords: Lagrangian scheme; symmetry-preserving; conservative; second order; multi-material compressible flow; cylindrical coordinates.

[1]Laboratory of Computational Physics, Institute of Applied Physics and Computational Mathematics, Beijing 100088, China. E-mail: cheng_juan@iapcm.ac.cn. Research is supported in part by NSFC grant 91130002. Additional support is provided by the National Basic Research Program of China under grant 2011CB309702 and CAEP under the project 2012A0202010.

[2]Division of Applied Mathematics, Brown University, Providence, RI 02912. E-mail: shu@dam.brown.edu. Research is supported in part by ARO grant W911NF-11-1-0091 and NSF grant DMS-1112700.

1 Introduction

The class of Lagrangian methods, which have the mesh moving with the local fluid velocity, is one of the main classes of numerical methods for simulating multi-material fluid flows. Since it has the distinguished advantage in capturing material interfaces automatically and sharply, it is widely used in many fields for multi-material flow simulations such as astrophysics, inertial confinement fusion (ICF) and computational fluid dynamics (CFD).

In many application fields such as ICF and astrophysics, there exist many three-dimensional cylindrical-symmetric models such as sphere-shape capsules and cylinder-shape hohlraum. This kind of models is usually simulated by Lagrangian methods in the two-dimensional cylindrical coordinates. For a Lagrangian scheme applied in these problems, one critical issue is how to maintain the spherical symmetry property in a cylindrical coordinate system, if the original physical problem has this symmetry. For example, in the simulation of implosions, a small deviation from spherical symmetry caused by numerical errors may be amplified by physical or numerical instabilities which may lead to unpredicted large errors. Numerous studies exist in the literature on this issue. In the past several decades, first order spherical-symmetry-preserving Lagrangian methods in two-dimensional cylindrical coordinates were well investigated. Among them, the most widely used method that keeps spherical symmetry exactly on an equal-angle-zoned grid in cylindrical coordinates is the area-weighted method, e.g. [20, 25, 24, 2, 4, 15, 1, 16, 19]. In this approach, in order to obtain the spherical symmetry property, a Cartesian form of the momentum equation is used in the cylindrical coordinate system, hence integration is performed on area rather than on the true volume in cylindrical coordinates. The main flaw of this kind of area-weighted schemes is that they may not maintain conservation for the momentum. Differently from the area-weighted schemes, Browne [3] presented a Lagrangian scheme termed "integrated total average" which is discretized on the true control volume. The scheme has been proven to be able to preserve the desired spherical symmetry in the two dimensional cylindrical geometry for equal-angle zoning. Unfortunately, this scheme can not keep the conservation of momen-

tum and total energy either. Margolin and Shashkov used a curvilinear grid to construct symmetry-preserving discretizations for Lagrangian gas dynamics [17]. In our recent work [7], a cell-centered Lagrangian scheme has been developed which is based on the control volume discretization. By compatible discretizations of the source term in the momentum equation, the scheme is designed to preserve one-dimensional spherical symmetry in a two-dimensional cylindrical geometry when computed on an equal-angle-zoned initial grid. A distinguished feature of the scheme is that it can keep both the properties of symmetry and conservation. In [8], we apply the methodology proposed in [7] to the first order control volume scheme of Maire in [15] to obtain the spherical symmetry property. The modified scheme can preserve several good properties such as symmetry, conservation and the geometric conservation law (GCL).

Although the issue on the symmetry-preserving property of the Lagrangian schemes has been well investigated, the situation is less satisfactory in terms of accuracy. Up to now, all the existing symmetry-preserving Lagrangian schemes are only first order accurate. In fact, to design a scheme with the preservation of spherical symmetry, not only the nodal velocity but also all the variables appearing in the integral of the numerical flux should be calculated symmetrically, which is especially difficult for a high order scheme to achieve. Moreover, a careful treatment must be performed on the source term, which has been the biggest obstacle for a Lagrangian scheme to be symmetry-preserving, even in the case of first order accuracy, and this is exactly the reason for most people to adopt the area-weighted schemes. It is quite challenging to design a higher than first order Lagrangian scheme with both the properties of spherical symmetry and conservation.

In this paper, we design a second order cell-centered Lagrangian scheme for solving Euler equations of compressible gas dynamics in cylindrical coordinates. The scheme is based on the control volume discretizations. It is uniformly second order accurate and is able to preserve one-dimensional spherical symmetry in a two-dimensional cylindrical geometry when computed on an equal-angle-zoned initial grid, and meanwhile it has many

other good properties such as conservation for mass, momentum and total energy and the GCL. Several two-dimensional numerical examples in cylindrical coordinates are presented to demonstrate the good performance of the scheme in terms of accuracy, symmetry, non-oscillation and robustness. The advantage of higher order accuracy is demonstrated in the numerical examples.

An outline of the rest of this paper is as follows. In Section 2, we describe our new second order symmetry-preserving Lagrangian scheme in two-dimensional cylindrical coordinates. In Section 3, we prove the symmetry-preserving property of the scheme. In Section 4, numerical examples are given to demonstrate the performance of the new Lagrangian scheme. In Section 4 we will give concluding remarks.

2 The design of a second order cell-centered symmetry-preserving Lagrangian scheme in cylindrical coordinates

2.1 The compressible Euler equations in a Lagrangian formulation in cylindrical coordinates

The compressible inviscid flow is governed by the Euler equations in the cylindrical coordinates which have the following integral form in the Lagrangian formulation

$$\begin{cases} \frac{\mathrm{d}}{\mathrm{d}t}\iint_{\Omega(t)}\rho r\mathrm{d}r\mathrm{d}z &= 0, \\ \frac{\mathrm{d}}{\mathrm{d}t}\iint_{\Omega(t)}\rho u_z r\mathrm{d}r\mathrm{d}z &= -\int_{\Gamma(t)} P n_z r\mathrm{d}l, \\ \frac{\mathrm{d}}{\mathrm{d}t}\iint_{\Omega(t)}\rho u_r r\mathrm{d}r\mathrm{d}z &= -\int_{\Gamma(t)} P n_r r\mathrm{d}l + \iint_{\Omega(t)} P\mathrm{d}r\mathrm{d}z, \\ \frac{\mathrm{d}}{\mathrm{d}t}\iint_{\Omega(t)}\rho E r\mathrm{d}r\mathrm{d}z &= -\int_{\Gamma(t)} P\mathbf{u}\cdot\mathbf{n} r\mathrm{d}l, \end{cases} \tag{2.1}$$

where z and r are the axial and radial directions respectively. ρ is density, P is pressure, E is the specific total energy. $\mathbf{u} = (u_z, u_r)$ where u_z and u_r are the velocity components in the z and r directions respectively, and $\mathbf{n} = (n_z, n_r)$ is the unit outward normal to the boundary $\Gamma(t)$ in the z-r coordinates. The equations present the conservation of mass, momentum and total energy.

The set of equations is completed by the addition of an equation of state (EOS) with the

following general form

$$P = P(\rho, e),$$

where $e = E - \frac{1}{2}|\mathbf{u}|^2$ is the specific internal energy. Especially, if we consider the ideal gas, then the equation of state has a simpler form

$$P = (\gamma - 1)\rho e,$$

where γ is a constant representing the ratio of specific heat capacities of the fluid.

The geometric conservation law refers to the fact that the rate of change of a Lagrangian volume should be computed consistently with the node motion, which can be formulated as

$$\frac{\mathrm{d}}{\mathrm{d}t}\iint_{\Omega(t)} \mathrm{d}V = \int_{\Gamma(t)} \mathbf{u}\cdot\mathbf{n}\mathrm{d}s. \tag{2.2}$$

2.2 The second order cell-centered symmetry-preserving Lagrangian scheme in cylindrical coordinates

2.2.1 Notations and assumptions

In this paper, we design our second order cell-centered Lagrangian scheme based on the framework of the first order cell-centered Lagrangian scheme developed in [15, 8]. We will also adopt notations in [15, 8]. The 2D spatial domain Ω is partitioned into quadrilateral computational cells. Each quadrilateral cell is denoted by Ω_c with a unique index c. The boundary of the cell Ω_c is denoted as $\partial\Omega_c$. Each vertex of the grid is appointed a unique index p and the counterclockwise ordered list of the vertices of the cell Ω_c is denoted by $p(c)$. A_c denotes the area of the cell Ω_c, and V_c denotes the volume of the cell obtained by rotating this cell around the azimuthal z-axis (without the 2π factor).

Based on these notations, we can rewrite the set of equations (2.1)-(2.2) in the following

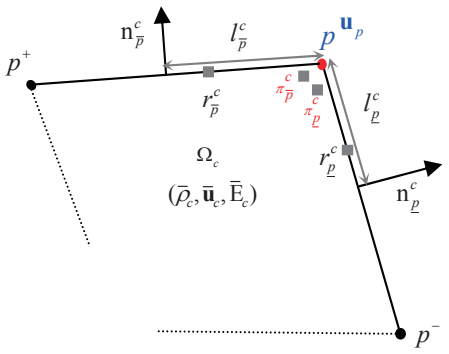

Figure 2.1: Denotation for the nodal variables.

control volume formulation

$$
\begin{aligned}
m_c \frac{\mathrm{d}}{\mathrm{d}t}\left(\frac{1}{\overline{\rho}_c}\right) &= \int_{\partial\Omega_c} \mathbf{u}\cdot\mathbf{n} r \mathrm{d}l, \\
m_c \frac{\mathrm{d}}{\mathrm{d}t}\overline{u}^c_z &= -\int_{\partial\Omega_c} P n_z r \mathrm{d}l, \\
m_c \frac{\mathrm{d}}{\mathrm{d}t}\overline{u}^c_r &= -\int_{\partial\Omega_c} P n_r r \mathrm{d}l + \iint_{\Omega_c} P \mathrm{d}r\mathrm{d}z, \\
m_c \frac{\mathrm{d}}{\mathrm{d}t}\overline{E}_c &= -\int_{\partial\Omega_c} P\mathbf{u}\cdot\mathbf{n} r \mathrm{d}l,
\end{aligned} \tag{2.3}
$$

where $m_c = \iint_{\Omega_c} \rho r \mathrm{d}r\mathrm{d}z$ denotes the mass in the cell Ω_c, which keeps constant during the time marching according to the first equation in (2.1). The first equation of (2.3) represents the geometric conservation law. $\overline{\rho}_c$, $\overline{\mathbf{u}}_c = (\overline{u}^c_z, \overline{u}^c_r)$ and $\overline{E}_c$ represent the cell averages of density, velocity and total energy in the cell Ω_c which are defined as follows

$$
\begin{aligned}
\overline{\rho}_c &= \frac{1}{V_c}\iint_{\Omega_c} \rho r \mathrm{d}r\mathrm{d}z, \qquad \overline{u}^c_z = \frac{1}{m_c}\iint_{\Omega_c} \rho u_z r \mathrm{d}r\mathrm{d}z, \\
\overline{u}^c_r &= \frac{1}{m_c}\iint_{\Omega_c} \rho u_r r \mathrm{d}r\mathrm{d}z, \quad \overline{E}_c = \frac{1}{m_c}\iint_{\Omega_c} \rho E r \mathrm{d}r\mathrm{d}z.
\end{aligned} \tag{2.4}
$$

The coordinates and velocity of the vertex p are denoted as (z_p, r_p) and $\mathbf{u}_p = (u^z_p, u^r_p)$ respectively. l_{pp^-} and l_{pp^+} denote the lengths of the edges $[p^-, p]$ and $[p, p^+]$, and $\mathbf{n}_{pp^-}$ and $\mathbf{n}_{pp^+}$ are the corresponding unit outward normals, where p^- and p^+ are the two neighboring vertices of the vertex p, see Figure 2.1.

Two nodal pressures at each vertex p are introduced to calculate the discrete gradient operators over the cell Ω_c which are denoted as $\pi^c_{\underline{p}}$ and $\pi^c_{\overline{p}}$ respectively, see Figure 2.1. These

two pressures are related to the two edges sharing the vertex p. The half lengths and the unit outward normals of the edges connected to the vertex p are denoted as follows

$$\begin{aligned} l^c_{\underline{p}} &= \frac{1}{2} l_{pp^-}, \quad l^c_{\overline{p}} = \frac{1}{2} l_{pp^+}, \\ \mathbf{n}^c_{\underline{p}} &= \mathbf{n}_{pp^-}, \quad \mathbf{n}^c_{\overline{p}} = \mathbf{n}_{pp^+}. \end{aligned} \tag{2.5}$$

The pseudo radii $r^c_{\underline{p}}$ and $r^c_{\overline{p}}$ are defined as

$$r^c_{\underline{p}} = \frac{1}{3}(2r_p + r_{p^-}), \quad r^c_{\overline{p}} = \frac{1}{3}(2r_p + r_{p^+}) \tag{2.6}$$

with which the GCL can be rewritten as the first equation of the following semi-discrete scheme (2.8) for the equations (2.3) [15].

Similarly, we denote

$$\begin{aligned} z^c_{\underline{p}} &= \frac{1}{3}(2z_p + z_{p^-}), \quad z^c_{\overline{p}} = \frac{1}{3}(2z_p + z_{p^+}), \\ \xi^c_{\underline{p}} &= \sqrt{(z^c_{\underline{p}})^2 + (r^c_{\underline{p}})^2}, \quad \xi^c_{\overline{p}} = \sqrt{(z^c_{\overline{p}})^2 + (r^c_{\overline{p}})^2}. \end{aligned} \tag{2.7}$$

2.2.2 Spatial discretization

The semi-discrete finite volume scheme for the governing equations (2.3) is described as follows,

$$\begin{aligned} & m_c \frac{\mathrm{d}}{\mathrm{d}t}\left(\frac{1}{\overline{\rho}_c}\right) - \sum_{p\in p(c)} (r^c_{\underline{p}} l^c_{\underline{p}} \mathbf{n}^c_{\underline{p}} + r^c_{\overline{p}} l^c_{\overline{p}} \mathbf{n}^c_{\overline{p}}) \cdot \mathbf{u}_p = 0, \\ & m_c \frac{\mathrm{d}}{\mathrm{d}t} \overline{u}^c_z + \sum_{p\in p(c)} (r^c_{\underline{p}} l^c_{\underline{p}} \pi^c_{\underline{p}} n^{c,z}_{\underline{p}} + r^c_{\overline{p}} l^c_{\overline{p}} \pi^c_{\overline{p}} n^{c,z}_{\overline{p}}) = 0, \\ & m_c \frac{\mathrm{d}}{\mathrm{d}t} \overline{u}^c_r + \sum_{p\in p(c)} (r^c_{\underline{p}} l^c_{\underline{p}} \pi^c_{\underline{p}} n^{c,r}_{\underline{p}} + r^c_{\overline{p}} l^c_{\overline{p}} \pi^c_{\overline{p}} n^{c,r}_{\overline{p}}) - A_c P_s = 0, \\ & m_c \frac{\mathrm{d}}{\mathrm{d}t} \overline{E}_c + \sum_{p\in p(c)} (r^c_{\underline{p}} l^c_{\underline{p}} \pi^c_{\underline{p}} \mathbf{n}^c_{\underline{p}} + r^c_{\overline{p}} l^c_{\overline{p}} \pi^c_{\overline{p}} \mathbf{n}^c_{\overline{p}}) \cdot \mathbf{u}_p = 0, \end{aligned} \tag{2.8}$$

where $\mathbf{n}^c_{\underline{p}} = (n^{c,z}_{\underline{p}}, n^{c,r}_{\underline{p}})$ and $\mathbf{n}^c_{\overline{p}} = (n^{c,z}_{\overline{p}}, n^{c,r}_{\overline{p}})$. In order to design a Lagrangian scheme with second order accuracy in space, all the variables such as $\pi^c_{\underline{p}}$, $\pi^c_{\overline{p}}$, $\mathbf{u}_p$ and P_s appearing in (2.8) should be approximated by second order reconstructions which will be discussed in the following subsection.

2.2.3 Computation of nodal pressure and velocity

The nodal pressures $\pi_{\underline{p}}^c$ and $\pi_{\overline{p}}^c$ are determined in the following way,

$$\begin{aligned}\pi_{\underline{p}}^c &= P_{\underline{p}}^c - z_{\underline{p}}^c(\mathbf{u}_p - \mathbf{u}_{\underline{p}}^c)\cdot\mathbf{n}_{\underline{p}}^c,\\ \pi_{\overline{p}}^c &= P_{\overline{p}}^c - z_{\overline{p}}^c(\mathbf{u}_p - \mathbf{u}_{\overline{p}}^c)\cdot\mathbf{n}_{\overline{p}}^c,\end{aligned} \tag{2.9}$$

where $P_{\underline{p}}^c$ and $P_{\overline{p}}^c$ are the pressure values at the vertex p which are determined by the nodal vectors $\{\rho_{\underline{p}}^c, \mathbf{u}_{\underline{p}}^c, E_{\underline{p}}^c\}$ and $\{\rho_{\overline{p}}^c, \mathbf{u}_{\overline{p}}^c, E_{\overline{p}}^c\}$ respectively. $\{\rho_{\underline{p}}^c, \mathbf{u}_{\underline{p}}^c, E_{\underline{p}}^c\}$ and $\{\rho_{\overline{p}}^c, \mathbf{u}_{\overline{p}}^c, E_{\overline{p}}^c\}$ will be obtained by a weighted essentially non-oscillatory (WENO) reconstruction, to be introduced in the next subsection. $z_{\underline{p}}^c$ and $z_{\overline{p}}^c$ are the mass fluxes swept by the waves which can be determined in several ways. In this paper, we will use the acoustic approach, that is

$$z_{\underline{p}}^c = \rho_{\underline{p}}^c a_{\underline{p}}^c, \quad z_{\overline{p}}^c = \rho_{\overline{p}}^c a_{\overline{p}}^c, \tag{2.10}$$

where $a_{\underline{p}}^c$ and $a_{\overline{p}}^c$ are the local isentropic speeds of sound at the vertex p which are obtained by $\{\rho_{\underline{p}}^c, \mathbf{u}_{\underline{p}}^c, E_{\underline{p}}^c\}$ and $\{\rho_{\overline{p}}^c, \mathbf{u}_{\overline{p}}^c, E_{\overline{p}}^c\}$ respectively.

In order to ensure the scheme to be conservative for the momentum and total energy, the following sufficient condition should be satisfied [15],

$$\sum_{c\in c(p)} (r_{\underline{p}}^c l_{\underline{p}}^c \pi_{\underline{p}}^c n_{\underline{p}}^{c,r} + r_{\overline{p}}^c l_{\overline{p}}^c \pi_{\overline{p}}^c n_{\overline{p}}^{c,r}) = 0, \tag{2.11}$$

where $c(p)$ is the set of cells around the vertex p. From (2.9) and (2.11), we can get the following specific formula to calculate the nodal velocity,

$$\mathbf{u}_p = M_p^{-1} \sum_{c\in c(p)} \{r_{\underline{p}}^c l_{\underline{p}}^c [P_{\underline{p}}^c \mathbf{n}_{\underline{p}}^c + z_{\underline{p}}^c \mathbf{u}_{\underline{p}}^c (\mathbf{n}_{\underline{p}}^c \otimes \mathbf{n}_{\underline{p}}^c)] + r_{\overline{p}}^c l_{\overline{p}}^c [P_{\overline{p}}^c \mathbf{n}_{\overline{p}}^c + z_{\overline{p}}^c \mathbf{u}_{\overline{p}}^c (\mathbf{n}_{\overline{p}}^c \otimes \mathbf{n}_{\overline{p}}^c)]\}, \tag{2.12}$$

where the 2×2 matrices M_{pc} and M_p are denoted as

$$M_{pc} = z_{\underline{p}}^c r_{\underline{p}}^c l_{\underline{p}}^c (\mathbf{n}_{\underline{p}}^c \otimes \mathbf{n}_{\underline{p}}^c) + z_{\overline{p}}^c r_{\overline{p}}^c l_{\overline{p}}^c (\mathbf{n}_{\overline{p}}^c \otimes \mathbf{n}_{\overline{p}}^c), \quad M_p = \sum_{c\in c(p)} M_{pc}. \tag{2.13}$$

Once the nodal velocity $\mathbf{u}_p$ at vertex p is determined, the cell vertex will move with the following local kinematic equation

$$\frac{\mathrm{d}}{\mathrm{d}t}\mathbf{x}_p = \mathbf{u}_p, \quad \mathbf{x}_p(0) = \mathbf{x}_p^0, \tag{2.14}$$

where $\mathbf{x}_p = (z_p, r_p)$ denotes the position of vertex p at $t > 0$ and $\mathbf{x}_p^0$ denotes its initial position.

To design a high order Lagrangian scheme with the spherical symmetry property, there are two key points that should be carefully considered. One is how to maintain the spherical symmetry property of the nodal variables such as pressure and velocity in the process of reconstruction. The other one is how to calculate the source term in a compatible way with the numerical flux so as to keep the momentum (cell-centered velocity) at the angular direction to be always zero when a one-dimensional spherical-symmetric problem is simulated. In the following two subsections, we will give a detailed description on these two issues.

Remark 1: For the nodes located on the z axis, due to the situation of $r = 0$, the determinant of the matrix M_p defined by (2.13) may become zero on a rectangular Cartesian grid. In this case, the system (2.12) for calculating the nodal velocity becomes unsolvable. To deal with this problem, we embed the boundary condition $u_p^r = 0$ into (2.12) directly when we calculate the velocity of nodes on the z axis. Then the system (2.12) can be simplified as a scalar nonsingular algebraic equation by which u_p^z is uniquely determined.

2.2.4 WENO reconstruction

In this paper, we will use the weighted essentially non-oscillatory (WENO) idea [14, 10] to reconstruct polynomial functions on each Ω_c based on the cell-average information of the cell Ω_c and its neighbors, by which the variables such as $\pi_{\underline{p}}^c$, $\pi_{\overline{p}}^c$, $\mathbf{u}_p$ and P_s shown in (2.8) can be approximated with second order accuracy.

Suppose we consider a one-dimensional spherical symmetric problem simulated on an equal-angled polar grid (see Figure 2.2), then we know the cell averages $\overline{\mathbf{U}}_c = (\overline{\rho}_c, \overline{\mathbf{u}}_c, \overline{E}_c)^T$ in the cell Ω_c are symmetric, that is, $\overline{\rho}_c, \overline{E}_c$ and the component of $\overline{\mathbf{u}}_c$ in the radial direction are the same in all cells with the same radial position, while the component of $\overline{\mathbf{u}}_c$ in the cell's angular direction is zero for all cells. Our goal is to reconstruct these variables to get second order approximation and meanwhile keep their symmetry property. In practice, unfortunately we find the symmetry is not easy to achieve especially in the cylindrical coordinates.

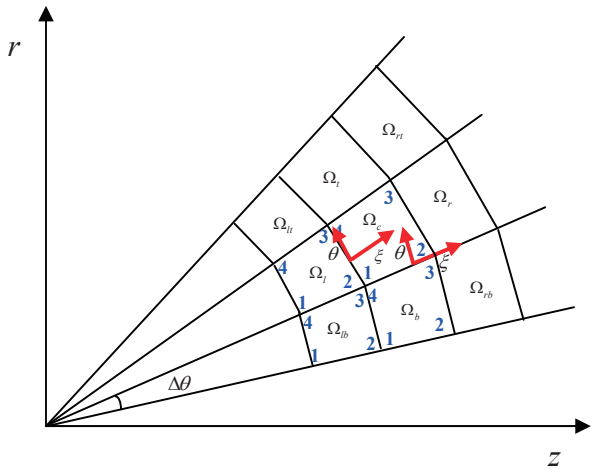

Figure 2.2: The local ξ-θ coordinates used in the WENO reconstruction.

The difficulties mainly lie in two aspects. One is that the components of $\overline{\mathbf{u}}_c$ in the z and r directions are not symmetric, which leads to a lack of symmetry for the candidate stencils used for the reconstruction. The other aspect is that the usual reconstruction is based on the integral of the conserved variables over the control volume which will involve the parameter r in the cylindrical coordinates (see the right hand side of (2.4)). As the r coordinate in the cells with the same radial position and different angular positions are different, the symmetry in the reconstruction cannot be maintained.

To overcome these difficulties, we take the following two procedures in the reconstruction. First, along each edge of the cell, we transform the cell averages of the variables in its neighboring cells which are involved in the reconstruction from its usual (z, r) coordinates to the local polar coordinates (ξ, θ), where ξ is the radial direction passing through the center of this edge and the origin, and θ is the angular direction which is counter-clockwisely orthogonal to ξ, see Figure 2.2 for an illustration. Secondly, to determine the coefficients of the reconstructed polynomials, we perform the integral on the area rather than on the volume so that the parameter r will not appear in the integral. This treatment will limit the reconstruction approximation to at most second order accuracy, but it will keep the symmetry of the reconstructed variables, and meanwhile it will not destroy the conservation property of the scheme since the sufficient condition (2.11) for conservation is still satisfied,

by which the nodal pressure and velocity $\pi_{\underline{p}}^c, \pi_{\overline{p}}^c, \mathbf{u}_p$ are determined.

To be more specific, the reconstruction is implemented in the left and right cells along each edge, by which the left and right values of the corresponding variables at the two vertices of this edge can be obtained. Suppose the reconstructed linear polynomial $\mathbf{U}_e^c(z,r) = (\rho_e^c(z,r), u_e^{c,\xi}(z,r), u_e^{c,\theta}(z,r), E_e^c(z,r))^T$ in the cell Ω_c along one of its edges $e, e = 1, ..., 4$ (we define the sequence of the cell's edges as those connecting the vertices "1" and "4", "2" and "3", "1" and "2", "3" and "4" respectively) is of the following form

$$\mathbf{U}_e^c(z,r) = \mathbf{a}_e^c(z - z_c) + \mathbf{b}_e^c(r - r_c) + \mathbf{c}_e^c,$$

where (z_c, r_c) denotes the coordinates of the cell center, and the coefficient vector $\{\mathbf{a}_e^c, \mathbf{b}_e^c, \mathbf{c}_e^c\}$ is determined by agreeing with the given cell averages on a 3-cell stencil including Ω_c, for example by

$$\begin{aligned} \iint_{\Omega_b} \mathbf{U}_e^c(z,r)dzdr &= \overline{\mathbf{U}}_b A_b, \\ \iint_{\Omega_c} \mathbf{U}_e^c(z,r)dzdr &= \overline{\mathbf{U}}_c A_c, \\ \iint_{\Omega_l} \mathbf{U}_e^c(z,r)dzdr &= \overline{\mathbf{U}}_l A_l, \end{aligned} \tag{2.15}$$

where A_c, A_b, A_l are the areas of the cells Ω_c, Ω_b and Ω_l (see Figure 2.2) respectively, and $\overline{\mathbf{U}}_c = (\overline{\rho}_c, \overline{\mathbf{u}}_c, \overline{E}_c)^T$, $\overline{\mathbf{U}}_b = (\overline{\rho}_b, \overline{\mathbf{u}}_b, \overline{E}_b)^T$ and $\overline{\mathbf{U}}_l = (\overline{\rho}_l, \overline{\mathbf{u}}_l, \overline{E}_l)^T$. Notice that the integral in (2.15) is performed on the area rather than on the usual control volume in order to maintain the symmetry of the reconstructed variables. This kind of reconstruction can be at most second order accurate.

In order to have an essentially non-oscillatory and symmetry-preserving algorithm, we use the idea of a simple WENO reconstruction. For the reconstruction on the cell Ω_c, we consider the following four sets of nonsingular stencils:

$$\{1 : \Omega_b, \Omega_c, \Omega_l\}; \quad \{2 : \Omega_l, \Omega_c, \Omega_t\}; \quad \{3 : \Omega_t, \Omega_c, \Omega_r\}; \quad \{4 : \Omega_r, \Omega_c, \Omega_b\}.$$

Denote $\{\mathbf{a}_{e,i}^c, \mathbf{b}_{e,i}^c, \mathbf{c}_{e,i}^c, i = 1, ..., 4\}$ to be the coefficients of linear polynomials reconstructed by the above four stencils respectively, then the coefficients $\{\mathbf{a}_e^c, \mathbf{b}_e^c, \mathbf{c}_e^c\}$ of the final reconstructed

polynomials are determined by

$$\mathbf{a}_e^c = \sum_{i=1}^{4} \mathbf{w}_i \mathbf{a}_{e,i}^c, \quad \mathbf{b}_e^c = \sum_{i=1}^{4} \mathbf{w}_i \mathbf{b}_{e,i}^c, \quad \mathbf{c}_e^c = \sum_{i=1}^{4} \mathbf{w}_i \mathbf{c}_{e,i}^c,$$

where the weights $\mathbf{w}_i$ are chosen as

$$\mathbf{w}_i = \frac{\tilde{\mathbf{w}}_i}{\sum_{j=1}^{4} \tilde{\mathbf{w}}_j}, \qquad \tilde{\mathbf{w}}_j = \frac{1}{[(|\mathbf{a}_{e,j}^c|^2 + |\mathbf{b}_{e,j}^c|^2)A_c + \epsilon]^2} \tag{2.16}$$

with $\epsilon = 10^{-6}$. This crude WENO reconstruction, which does not theoretically increase the accuracy of each candidate stencil but is very easy to compute and can preserve the symmetry, also performs nicely in our numerical experiments.

The density, velocity and energy at the four vertices of the cell Ω_c are then obtained by the reconstructed polynomials $\{\mathbf{U}_e^c(z,r), e = 1, ..., 4\}$, that is,

$$\begin{cases} (\rho_{\underline{1}}^c, \mathbf{u}_{\underline{1}}^c, E_{\underline{1}}^c) = \mathbf{U}_1^c(z_1^c, r_1^c), & (\rho_{\underline{4}}^c, \mathbf{u}_{\underline{4}}^c, E_{\underline{4}}^c) = \mathbf{U}_1^c(z_4^c, r_4^c), \\ (\rho_{\underline{2}}^c, \mathbf{u}_{\underline{2}}^c, E_{\underline{2}}^c) = \mathbf{U}_2^c(z_2^c, r_2^c), & (\rho_{\underline{3}}^c, \mathbf{u}_{\underline{3}}^c, E_{\underline{3}}^c) = \mathbf{U}_2^c(z_3^c, r_3^c), \\ (\rho_{\overline{1}}^c, \mathbf{u}_{\overline{1}}^c, E_{\overline{1}}^c) = \mathbf{U}_3^c(z_1^c, r_1^c), & (\rho_{\underline{2}}^c, \mathbf{u}_{\underline{2}}^c, E_{\underline{2}}^c) = \mathbf{U}_3^c(z_2^c, r_2^c), \\ (\rho_{\overline{3}}^c, \mathbf{u}_{\overline{3}}^c, E_{\overline{3}}^c) = \mathbf{U}_4^c(z_3^c, r_3^c), & (\rho_{\underline{4}}^c, \mathbf{u}_{\underline{4}}^c, E_{\underline{4}}^c) = \mathbf{U}_4^c(z_4^c, r_4^c). \end{cases}$$

Similarly, we can get the reconstructed polynomials in the cell at the other side of the edge from which we can get the density, velocity and energy at its vertices. For a one-dimensional spherical symmetric problem simulated on an equal-angled polar grid, due to the symmetric structure of the stencils and the way to determine the coefficients (2.16), the following symmetry relationships for the nodal variables hold by the previously described WENO reconstruction,

$$\begin{cases} \rho_{\underline{1}}^c = \rho_{\overline{4}}^c = \rho_{\underline{1}}^b = \rho_{\overline{4}}^b, & \rho_{\overline{1}}^c = \rho_{\underline{4}}^c = \rho_{\overline{1}}^b = \rho_{\underline{4}}^b, \\ \rho_{\underline{2}}^c = \rho_{\overline{3}}^c = \rho_{\underline{2}}^b = \rho_{\overline{3}}^b, & \rho_{\overline{2}}^c = \rho_{\underline{3}}^c = \rho_{\overline{2}}^b = \rho_{\underline{3}}^b, \\ E_{\underline{1}}^c = E_{\overline{4}}^c = E_{\underline{1}}^b = E_{\overline{4}}^b, & E_{\overline{1}}^c = E_{\underline{4}}^c = E_{\overline{1}}^b = E_{\underline{4}}^b, \\ E_{\underline{2}}^c = E_{\overline{3}}^c = E_{\underline{2}}^b = E_{\overline{3}}^b, & E_{\overline{2}}^c = E_{\underline{3}}^c = E_{\overline{2}}^b = E_{\underline{3}}^b, \end{cases} \tag{2.17}$$

and

$$\begin{cases} (u^\xi)_{\underline{1}}^c = (u^\xi)_{\overline{4}}^c = (u^\xi)_{\underline{1}}^b = (u^\xi)_{\overline{4}}^b, & (u^\xi)_{\overline{1}}^c = (u^\xi)_{\underline{4}}^c = (u^\xi)_{\overline{1}}^b = (u^\xi)_{\underline{4}}^b, \\ (u^\xi)_{\underline{2}}^c = (u^\xi)_{\overline{3}}^c = (u^\xi)_{\underline{2}}^b = (u^\xi)_{\overline{3}}^b, & (u^\xi)_{\underline{2}}^c = (u^\xi)_{\overline{3}}^c = (u^\xi)_{\underline{2}}^b = (u^\xi)_{\overline{3}}^b, \\ (u^\theta)_{\underline{1}}^c = (u^\theta)_{\overline{4}}^c = (u^\theta)_{\underline{1}}^b = (u^\theta)_{\overline{4}}^b = 0, & (u^\theta)_{\overline{1}}^c = (u^\theta)_{\underline{4}}^c = (u^\theta)_{\overline{1}}^b = (u^\theta)_{\underline{4}}^b = 0, \\ (u^\theta)_{\underline{2}}^c = (u^\theta)_{\overline{3}}^c = (u^\theta)_{\underline{2}}^b = (u^\theta)_{\overline{3}}^b = 0, & (u^\theta)_{\overline{2}}^c = (u^\theta)_{\underline{3}}^c = (u^\theta)_{\overline{2}}^b = (u^\theta)_{\underline{3}}^b = 0, \end{cases} \tag{2.18}$$

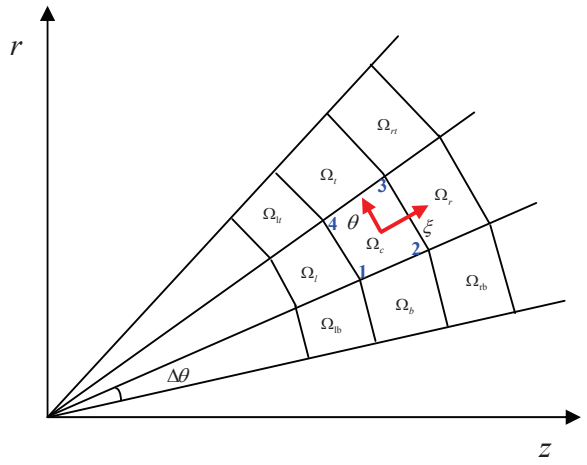

Figure 2.3: The local ξ-θ coordinates used for the proof of symmetry preservation for the conserved variables on the equal-angular polar grid.

where (ξ, θ) denotes the cell's local polar coordinates (see Figure 2.3) which are the same as those for the edges '1' and '2' for an equal-angled polar grid. As to $\{z_{\underline{p}}^c, z_{\overline{p}}^c, P_{\underline{p}}^c, P_{\overline{p}}^c\}$, since they are determined by $\{\rho_{\underline{p}}^c, \rho_{\overline{p}}^c, \mathbf{u}_{\underline{p}}^c, \mathbf{u}_{\overline{p}}^c, E_{\underline{p}}^c, E_{\overline{p}}^c\}$, they also have the same symmetry property.

Remark 2: In the procedure of the WENO reconstruction, for some test problems with strong discontinuities, the method of local characteristic decomposition should be applied to avoid the appearance of spurious oscillation. We refer to [23] for the details of the Roe-type characteristic decomposition that we have used in this paper. The method of local characteristic decomposition should be performed along the normal direction of the cell's edges, that is why we accomplish the previous WENO reconstruction along each edge of the cell. The application of these local characteristic decompositions does not affect the symmetry-preserving property.

2.2.5 Computation of the source term

In order to design a control volume Lagrangian scheme with the spherical symmetry property, the source term should be carefully discretized. For a second order Lagrangian scheme, P_s in the source term should be determined as

$$P_s = \frac{\xi_{\overline{1}}^c \pi_{\overline{1}}^c + \xi_{\underline{2}}^c \pi_{\underline{2}}^c + \xi_{\overline{3}}^c \pi_{\overline{3}}^c + \xi_{\underline{4}}^c \pi_{\underline{4}}^c}{\xi_{\overline{1}}^c + \xi_{\underline{2}}^c + \xi_{\overline{3}}^c + \xi_{\underline{4}}^c}, \tag{2.19}$$

where $\pi^c_{\overline{1}}$, $\pi^c_{\underline{2}}$, $\pi^c_{\overline{3}}$ and $\pi^c_{\underline{4}}$ are the values of pressure related to the two radial edges of the cell Ω_c (see Figure 2.3). $\xi^c_{\overline{1}}, \xi^c_{\underline{2}}, \xi^c_{\overline{3}}$ and $\xi^c_{\underline{4}}$ are defined as (2.7). In the next section we will prove that the scheme with such choice of the source term can keep spherical symmetry.

2.2.6 Time discretization

The Euler forward time discretization for the equation of nodal movement (2.14) is given as follows

$$\begin{aligned} z_p^{n+1} &= z_p^n + \Delta t^n u_p^{z,n}, \\ r_p^{n+1} &= r_p^n + \Delta t^n u_p^{r,n}, \end{aligned} \tag{2.20}$$

where $u_p^{z,n}, u_p^{r,n}$ are the z and r components of $\mathbf{u}_p$ at the n-th time step.

By the semi-discrete scheme (2.8), the following fully discretized scheme can be obtained by the Euler forward time discretization,

$$\begin{aligned} & m_c \begin{pmatrix} \frac{1}{\overline{\rho}_c^{n+1}} - \frac{1}{\overline{\rho}_c^n} \\ \overline{u}_c^{z,n+1} - \overline{u}_c^{z,n} \\ \overline{u}_c^{r,n+1} - \overline{u}_c^{r,n} \\ \overline{E}_c^{n+1} - \overline{E}_c^n \end{pmatrix} \\ = \; & \Delta t^n \left(- \begin{pmatrix} -\sum_{p\in p(c)} (r^{c,n}_{\underline{p}} l^{c,n}_{\underline{p}} \mathbf{n}^{c,n}_{\underline{p}} + r^{c,n}_{\overline{p}} l^{c,n}_{\overline{p}} \mathbf{n}^{c,n}_{\overline{p}}) \cdot \mathbf{u}_p^n \\ \sum_{p\in p(c)} (r^{c,n}_{\underline{p}} l^{c,n}_{\underline{p}} \pi^{c,n}_{\underline{p}} n^{c,z,n}_{\underline{p}} + r^{c,n}_{\overline{p}} l^{c,n}_{\overline{p}} \pi^{c,n}_{\overline{p}} n^{c,z,n}_{\overline{p}}) \\ \sum_{p\in p(c)} (r^{c,n}_{\underline{p}} l^{c,n}_{\underline{p}} \pi^{c,n}_{\underline{p}} n^{c,r,n}_{\underline{p}} + r^{c,n}_{\overline{p}} l^{c,n}_{\overline{p}} \pi^{c,n}_{\overline{p}} n^{c,r,n}_{\overline{p}}) \\ \sum_{p\in p(c)} (r^{c,n}_{\underline{p}} l^{c,n}_{\underline{p}} \pi^{c,n}_{\underline{p}} \mathbf{n}^{c,n}_{\underline{p}} + r^{c,n}_{\overline{p}} l^{c,n}_{\overline{p}} \pi^{c,n}_{\overline{p}} \mathbf{n}^{c,n}_{\overline{p}}) \cdot \mathbf{u}_p^n \end{pmatrix} + \begin{pmatrix} 0 \\ 0 \\ A_c^n P_s^n \\ 0 \end{pmatrix} \right). \end{aligned} \tag{2.21}$$

Here the variables with the superscripts "n" and "$n+1$" represent the values of the corresponding variables at the n-th and $(n+1)$-th time steps respectively. $\pi^c_{\underline{p}}, \pi^c_{\overline{p}}, \mathbf{u}_p, P_s$ are obtained by the WENO reconstruction introduced in the previous subsection. The scheme (2.21) then has first order accuracy in time and second order accuracy in space.

To design a Lagrangian scheme with uniformly second order accuracy both in space and time, the time marching is implemented by a second order total variation diminishing (TVD), or strong stability preserving (SSP) Runge-Kutta type method [22] which has the following form in the Lagrangian formulation [6].

Stage 1,

$$z_p^{(1)} = z_p^n + \Delta t^n u_p^{z,n}, \quad r_p^{(1)} = r_p^n + \Delta t^n u_p^{r,n},$$
$$\overline{\mathbf{U}}_c^{(1)} = \overline{\mathbf{U}}_c^n + \frac{\Delta t^n}{m_c}\mathbf{L}(\overline{\mathbf{U}}_c^n); \tag{2.22}$$

Stage 2,

$$z_p^{n+1} = \frac{1}{2}z_p^n + \frac{1}{2}[z_p^{(1)} + \Delta t^n u_p^{z,(1)}], \quad r_p^{n+1} = \frac{1}{2}r_p^n + \frac{1}{2}[r_p^{(1)} + \Delta t^n u_p^{r,(1)}],$$
$$\overline{\mathbf{U}}_c^{n+1} = \frac{1}{2}\overline{\mathbf{U}}_c^n + \frac{1}{2}[\overline{\mathbf{U}}_c^{(1)} + \frac{\Delta t^n}{m_c}\mathbf{L}(\overline{\mathbf{U}}_c^{(1)})]; \tag{2.23}$$

where $\mathbf{U}_c = (\frac{1}{\overline{\rho}_c}, \overline{u}_z^c, \overline{u}_r^c, \overline{E}_c)^T$ and $\mathbf{L}$ is the numerical spatial operator representing the right hand of the scheme (2.21).

Notice that the SSP Runge-Kutta scheme is a convex combination of Euler forward time stepping, and is hence conservative, stable and symmetry-preserving whenever the Euler forward time stepping is conservative, stable and symmetry-preserving.

The time step Δt^n is controlled by both the CFL condition and the criterion on the variation of the volume. The CFL condition is satisfied as follows

$$\Delta t_e = C_e \min_c \{l_c^n / (|\overline{\mathbf{u}}_c^n| + a_c^n)\},$$

where l_c^n is the length of the shortest edge of the cell Ω_c, and a_c^n is the sound speed determined by the cell averages within this cell. C_e is the Courant number which is set to be 0.5 unless otherwise stated in the following tests.

The criterion on the variation of the volume is determined by

$$\Delta t_v = C_v \left\{ \frac{V_c^n}{|\frac{d}{dt}V_c(t^n)|} \right\},$$

where $\frac{d}{dt}V_c(t^n) = \frac{V_c^{n+1} - V_c^n}{\Delta t^n}$. The parameter $C_v = 0.1$ is used in the numerical simulations.

Finally, the time step Δt^n is given by

$$\Delta t^n = \min(\Delta t_e, \Delta t_v).$$

3 The proof of the spherical-symmetry-preserving property

In this section, we will prove the scheme (2.22)-(2.23) can keep the spherical symmetry property computed on an equal-angle-zoned initial grid.

Theorem: *The scheme (2.22)-(2.23) can keep the one-dimensional spherical symmetry property computed on an equal-angle zoned initial grid. That is, if the solution has one-dimensional spherical symmetry at the initial time, then the computational solution will keep this symmetry with the time marching.*

Proof: Since the SSP Runge-Kutta scheme (2.22)-(2.23) is a convex combination of Euler forward time stepping, it is symmetry-preserving if the scheme (2.21) is symmetry-preserving. Thus we only need to prove the scheme (2.21) is symmetry-preserving. Without loss of generality, we only need to prove the solution of the scheme (2.21) can keep the spherical symmetry at the $(n+1)$-th time step, if it is known to be spherical symmetric at the n-th time step. Notice that, for the Lagrangian solution, symmetry preserving refers to the evolution of both the conserved variables and the grid. For the convenience of notation, we adopt the convention that variables without the superscript "$n+1$" are those at the n-th time step.

To facilitate the proof of the symmetry property, in the following, we simplify the vertex indices of all the cells as $p = 1, 2, 3, 4$ (shown in Figure 3.1 and Figure 2.3).

1. **The proof of grid symmetry preservation.**

   Without loss of the generality, we consider the velocity of the vertex p which connects the cells $\Omega_c, \Omega_b, \Omega_{lb}$ and Ω_l (see Figure 3.1). For the convenience of proof, in the following, we will project all the variables relative to the determination of the nodal velocity to its local polar coordinates (see Figure 3.1). Thus the outward normal direction of the four edges connected to the vertex p in the local ξ-θ coordinates can

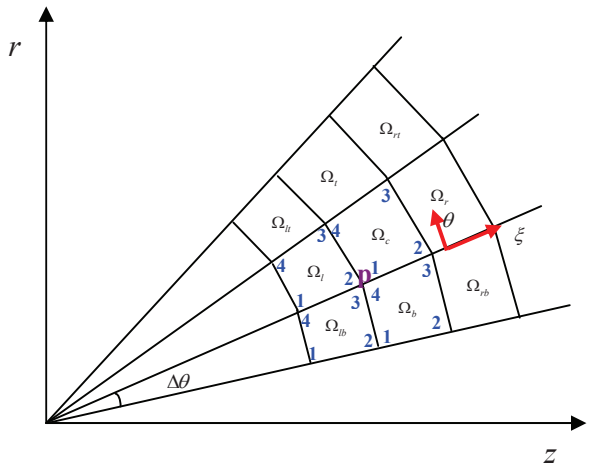

Figure 3.1: The local ξ-θ coordinates used for the proof of grid symmetry preservation on the equal-angular polar grid.

be written as

$$\mathbf{n}_{\underline{2}}^{l} = -\mathbf{n}_{\underline{1}}^{c} = \left(\cos\frac{\Delta\theta}{2}, \sin\frac{\Delta\theta}{2}\right), \quad \mathbf{n}_{\underline{3}}^{lb} = -\mathbf{n}_{\underline{4}}^{b} = \left(\cos\frac{\Delta\theta}{2}, -\sin\frac{\Delta\theta}{2}\right),$$
$$\mathbf{n}_{\overline{3}}^{lb} = \mathbf{n}_{\underline{4}}^{b} = -\mathbf{n}_{\overline{1}}^{c} = -\mathbf{n}_{\underline{2}}^{l} = (0, 1),$$

where $\Delta\theta$ is the angle between the two neighboring radial edges.

Assume that at the n-th time step the grid is a polar grid with equal angles and the cell averages of the conserved variables including density, momentum (velocity) and total energy are symmetric on this grid, namely these variables in the cells with the same radial position are identical. By the relationship (2.17)-(2.18) obtained by the precess of the WENO reconstruction, we can get symmetric reconstructed values of the variables at the vertex p in its four connected cells in the local ξ-θ coordinates. Specifically we denote them as,

$$\begin{cases} \rho_{\underline{1}}^{c} = \rho_{\underline{4}}^{b} = \rho_1, & \rho_{\overline{1}}^{c} = \rho_{\underline{4}}^{b} = \rho_2, & \rho_{\overline{3}}^{lb} = \rho_{\underline{2}}^{l} = \rho_3^{l}, & \rho_{\underline{3}}^{lb} = \rho_{\overline{2}}^{l} = \rho_4^{l}, \\ z_{\underline{1}}^{c} = z_{\underline{4}}^{b} = z_1, & z_{\overline{1}}^{c} = z_{\underline{4}}^{b} = z_2, & z_{\overline{3}}^{lb} = z_{\underline{2}}^{l} = z_3^{l}, & z_{\underline{3}}^{lb} = z_{\overline{2}}^{l} = z_4^{l}, \\ P_{\underline{1}}^{c} = P_{\underline{4}}^{b} = P_1, & P_{\overline{1}}^{c} = P_{\underline{4}}^{b} = P_2, & P_{\overline{3}}^{lb} = P_{\underline{2}}^{l} = P_3^{l}, & P_{\underline{3}}^{lb} = P_{\overline{2}}^{l} = P_4^{l}, \end{cases} \tag{3.1}$$

and

$$\begin{cases} \mathbf{u}_{\underline{1}}^{c} = u_1(\cos\frac{\Delta\theta}{2}, \sin\frac{\Delta\theta}{2}), & \mathbf{u}_{\underline{4}}^{b} = u_1(\cos\frac{\Delta\theta}{2}, -\sin\frac{\Delta\theta}{2}), \\ \mathbf{u}_{\overline{1}}^{c} = u_2(\cos\frac{\Delta\theta}{2}, \sin\frac{\Delta\theta}{2}), & \mathbf{u}_{\underline{4}}^{b} = u_2(\cos\frac{\Delta\theta}{2}, -\sin\frac{\Delta\theta}{2}), \\ \mathbf{u}_{\underline{2}}^{l} = u_3^{l}(\cos\frac{\Delta\theta}{2}, \sin\frac{\Delta\theta}{2}), & \mathbf{u}_{\overline{3}}^{lb} = u_3^{l}(\cos\frac{\Delta\theta}{2}, -\sin\frac{\Delta\theta}{2}), \\ \mathbf{u}_{\overline{2}}^{l} = u_4^{l}(\cos\frac{\Delta\theta}{2}, \sin\frac{\Delta\theta}{2}), & \mathbf{u}_{\underline{3}}^{lb} = u_4^{l}(\cos\frac{\Delta\theta}{2}, -\sin\frac{\Delta\theta}{2}), \end{cases} \tag{3.2}$$

where $\{\rho_i, z_i, P_i, u_i, i = 1, 2\}$ and $\{\rho_i^l, z_i^l, P_i^l, u_i^l, i = 3, 4\}$ only depend on the ξ coordinate and not on the θ coordinate.

In the case of a one-dimensional spherical flow computed on an equal angled polar grid, substituting (3.1)-(3.2) into (2.12)-(2.13), then we can get the velocity at the vertex p in its local ξ-θ coordinates in the following form

$$u_p^\xi = \frac{z_1 u_1 + z_4^l u_4^l - (P_1 - P_4^l)}{(z_1 + z_4^l)\cos\frac{\Delta\theta}{2}}, \quad u_p^\theta = 0. \tag{3.3}$$

Since $u_p^\theta = 0$ and u_p^ξ depends only on the ξ coordinate, we can conclude that the vertex velocity is symmetric.

2. **The proof of symmetry preservation for the conserved variables.**

We would need to prove the symmetry preservation of the evolved variables such as density, cell velocity and total energy.

We first rewrite the momentum equations in (2.8) and (2.21) along the cell's local ξ-θ coordinates (see Figure 2.3). The rewritten semi-discrete scheme is of the following form

$$\begin{aligned}
m_c \frac{\mathrm{d}}{\mathrm{d}t}\left(\frac{1}{\overline{\rho}_c}\right) &= \sum_{p=1,4} (r_{\underline{p}}^c l_{\underline{p}}^c \mathbf{n}_{\underline{p}}^c + r_{\overline{p}}^c l_{\overline{p}}^c \mathbf{n}_{\overline{p}}^c) \cdot \mathbf{u}_p, \\
m_c \frac{\mathrm{d}}{\mathrm{d}t}\overline{u}_c^\xi &= -\sum_{p=1,4} (r_{\underline{p}}^c l_{\underline{p}}^c \pi_{\underline{p}}^c n_{\underline{p}}^{c,\xi} + r_{\overline{p}}^c l_{\overline{p}}^c \pi_{\overline{p}}^c n_{\overline{p}}^{c,\xi}) + A_c P_s \sin\theta_c, \\
m_c \frac{\mathrm{d}}{\mathrm{d}t}\overline{u}_c^\theta &= -\sum_{p=1,4} (r_{\underline{p}}^c l_{\underline{p}}^c \pi_{\underline{p}}^c n_{\underline{p}}^{c,\theta} + r_{\overline{p}}^c l_{\overline{p}}^c \pi_{\overline{p}}^c n_{\overline{p}}^{c,\theta}) + A_c P_s \cos\theta_c, \\
m_c \frac{\mathrm{d}}{\mathrm{d}t}\overline{E}_c &= -\sum_{p=1,4} (r_{\underline{p}}^c l_{\underline{p}}^c \pi_{\underline{p}}^c \mathbf{n}_{\underline{p}}^c + r_{\overline{p}}^c l_{\overline{p}}^c \pi_{\overline{p}}^c \mathbf{n}_{\overline{p}}^c) \cdot \mathbf{u}_p,
\end{aligned} \tag{3.4}$$

where ξ is the radial direction passing through the cell center and the origin, and θ is the angular direction which is counter-clockwisely orthogonal to ξ. u_c^ξ and u_c^θ are values of the velocity components in the local ξ and θ directions respectively, $n_{\underline{p}}^{c,\xi}, n_{\overline{p}}^{c,\xi}$ and $n_{\underline{p}}^{c,\theta}, n_{\overline{p}}^{c,\theta}$ are the components of $\mathbf{n}_{\underline{p}}^c$ and $\mathbf{n}_{\overline{p}}^c$ along the ξ and θ directions respectively. θ_c is set to be the angle between the local ξ direction and the z coordinate.

In the following, we will project all the variables relative to the determination of the nodal pressure and velocity to the cell's local ξ-θ coordinates for the convenience of proof. Thus the outward normal direction of the cell's four edges in the local ξ-θ coordinates are as follows

$$\mathbf{n}_{12} = \left(-\sin\frac{\Delta\theta}{2}, -\cos\frac{\Delta\theta}{2}\right), \quad \mathbf{n}_{23} = (1,0),$$
$$\mathbf{n}_{34} = \left(-\sin\frac{\Delta\theta}{2}, \cos\frac{\Delta\theta}{2}\right), \qquad \mathbf{n}_{41} = (-1,0).$$

Denote the length of the four edges of the cell Ω_c as

$$l_{41} = l_1, \quad l_{23} = l_2, \quad l_{12} = l_3, \quad l_{34} = l_4.$$

Also denote the radial distances of the four vertices as $\{\xi_i, i = 1, ..., 4\}$. For the equal-angled grid, we have $l_4 = l_3$ and $\xi_4 = \xi_1, \xi_3 = \xi_2$.

From (2.17)-(2.18), we can denote the reconstructed values of the variables at the cell's four vertices as,

$$\begin{cases} \rho^c_{\underline{1}} = \rho^c_{\underline{4}} = \rho_1, & \rho^c_{\overline{1}} = \rho^c_{\underline{4}} = \rho_2, & \rho^c_{\underline{2}} = \rho^c_{\overline{3}} = \rho_3, & \rho^c_{\overline{2}} = \rho^c_{\underline{3}} = \rho_4, \\ z^c_{\underline{1}} = z^c_{\overline{4}} = z_1, & z^c_{\overline{1}} = z^c_{\underline{4}} = z_2, & z^c_{\underline{2}} = z^c_{\overline{3}} = z_3, & z^c_{\overline{2}} = z^c_{\underline{3}} = z_4, \\ P^c_{\underline{1}} = P^c_{\overline{4}} = P_1, & P^c_{\overline{1}} = P^c_{\underline{4}} = P_2, & P^c_{\underline{2}} = P^c_{\overline{3}} = P_3, & P^c_{\overline{2}} = P^c_{\underline{3}} = P_4, \end{cases} \tag{3.5}$$

$$\begin{cases} \mathbf{u}^c_{\underline{1}} = \mathbf{u}^c_{\overline{4}} = u_1(1,0), & \mathbf{u}^c_{\overline{1}} = \mathbf{u}^c_{\underline{4}} = u_2(1,0), \\ \mathbf{u}^c_{\underline{2}} = \mathbf{u}^c_{\overline{3}} = u_3(1,0), & \mathbf{u}^c_{\overline{2}} = \mathbf{u}^c_{\underline{3}} = u_4(1,0). \end{cases} \tag{3.6}$$

Similarly, the nodal values of the corresponding variables in the neighboring cells can also be denoted as,

$$\begin{cases} \rho^l_{\overline{2}} = \rho^l_4, & z^l_{\overline{2}} = z^l_4, & P^l_{\overline{2}} = P^l_4, & \mathbf{u}^l_{\overline{2}} = u^l_4(1,0), \\ \rho^r_{\underline{1}} = \rho^r_1, & z^r_{\underline{1}} = z^r_1, & P^r_{\underline{1}} = P^r_1, & \mathbf{u}^r_{\underline{1}} = u^r_1(1,0), \end{cases} \tag{3.7}$$

where $\{\rho_i, P_i, z_i, u_i, i = 1, ..., 4\}$ and $\{\rho^l_4, P^l_4, z^l_4, u^l_4, \rho^r_1, P^r_1, z^r_1, u^r_1\}$ depend only on the ξ coordinate and not on the θ coordinate, due to the symmetry-preserving process of the WENO reconstruction.

Similar to the formula (3.3), we can rewrite the velocity of the cell's four vertices in the local ξ-θ coordinates,

$$\begin{aligned}
\mathbf{u}_1 &= \frac{z_1 u_1 + z_4^l u_4^l - (P_1 - P_4^l)}{(z_1 + z_4^l)\cos\frac{\Delta\theta}{2}} \left(\cos\frac{\Delta\theta}{2}, -\sin\frac{\Delta\theta}{2}\right), \\
\mathbf{u}_2 &= \frac{z_4 u_4 + z_1^r u_1^r - (P_1^r - P_4)}{(z_4 + z_1^r)\cos\frac{\Delta\theta}{2}} \left(\cos\frac{\Delta\theta}{2}, -\sin\frac{\Delta\theta}{2}\right), \\
\mathbf{u}_3 &= \frac{z_4 u_4 + z_1^r u_1^r - (P_1^r - P_4)}{(z_4 + z_1^r)\cos\frac{\Delta\theta}{2}} \left(\cos\frac{\Delta\theta}{2}, \sin\frac{\Delta\theta}{2}\right), \\
\mathbf{u}_4 &= \frac{z_1 u_1 + z_4^l u_4^l - (P_1 - P_4^l)}{(z_1 + z_4^l)\cos\frac{\Delta\theta}{2}} \left(\cos\frac{\Delta\theta}{2}, \sin\frac{\Delta\theta}{2}\right).
\end{aligned} \tag{3.8}$$

Next we will try to write out each variable which appears at the right-hand side of (3.4) in details based on the previous denotations. By a simple manipulation, the nodal pressures appearing on the right hand side of the scheme (3.4) can be obtained as follows,

$$\begin{aligned}
\pi_{\underline{1}}^c &= P_{\underline{1}}^c - z_{\underline{1}}^c(\mathbf{u}_1 - \mathbf{u}_{\underline{1}}^c)\cdot\mathbf{n}_{41} = \frac{z_1 P_4^l + z_4^l P_1 - z_1 z_4^l(u_1 - u_4^l)}{z_1 + z_4^l}, \\
\pi_{\overline{1}}^c &= P_{\overline{1}}^c - z_{\overline{1}}^c(\mathbf{u}_1 - \mathbf{u}_{\overline{1}}^c)\cdot\mathbf{n}_{12} = P_2 - z_2 u_2 \sin\frac{\Delta\theta}{2}.
\end{aligned} \tag{3.9}$$

Thus we can denote

$$\begin{aligned}
\pi_{\underline{4}}^c &= \pi_{\overline{1}}^c = P_2 - z_2 u_2 \sin\frac{\Delta\theta}{2}, \\
\pi_{\underline{2}}^c &= \pi_{\overline{3}}^c = P_3 - z_3 u_3 \sin\frac{\Delta\theta}{2}, \\
\pi_{\overline{4}}^c &= \pi_{\underline{1}}^c = \frac{z_1 P_4^l + z_4^l P_1 - z_1 z_4^l(u_1 - u_4^l)}{z_1 + z_4^l}, \\
\pi_{\overline{2}}^c &= \pi_{\underline{3}}^c = \frac{z_1^r P_4 + z_4 P_1^r - z_1^r z_4(u_1^r - u_4)}{z_4 + z_1^r}.
\end{aligned} \tag{3.10}$$

For the simplicity of description, we denote

$$
\begin{aligned}
P_2^c &= P_2 - z_2 u_2 \sin\frac{\Delta\theta}{2},\\
P_3^c &= P_3 - z_3 u_3 \sin\frac{\Delta\theta}{2},\\
P_1^c &= \frac{z_1 P_4^l + z_4^l P_1 - z_1 z_4^l (u_1 - u_4^l)}{z_1 + z_4^l},\\
P_4^c &= \frac{z_1^r P_4 + z_4 P_1^r - z_1^r z_4 (u_1^r - u_4)}{z_4 + z_1^r},\\
u_1^c &= \frac{z_1 u_4^l + z_4^l u_1 - (P_1 - P_4^l)}{z_1 + z_4^l},\\
u_4^c &= \frac{z_1^r u_4 + z_4 u_1^r - (P_1^r - P_4)}{z_4 + z_1^r}.
\end{aligned}
$$

By the formula (2.19), we have

$$
P_s = \frac{(2\xi_1 + \xi_2) P_2^c + (\xi_1 + 2\xi_2) P_3^c}{3(\xi_1 + \xi_2)}. \tag{3.11}
$$

Other variables appearing at the right hand side of (3.4) can be described in the following details

$$
\begin{aligned}
& l_{\underline{1}}^c = l_{\underline{4}}^c = \frac{1}{2} l_1, \quad l_{\overline{1}}^c = l_{\underline{2}}^c = l_{\overline{3}}^c = l_{\underline{4}}^c = \frac{1}{2} l_3, \quad l_{\overline{2}}^c = l_{\underline{3}}^c = \frac{1}{2} l_2,\\
& (n_{\underline{1}}^{c,\xi}, n_{\underline{1}}^{c,\theta}) = (n_{\overline{4}}^{c,\xi}, n_{\overline{4}}^{c,\theta}) = \mathbf{n}_{41} = (-1, 0),\\
& (n_{\underline{2}}^{c,\xi}, n_{\underline{2}}^{c,\theta}) = (n_{\overline{1}}^{c,\xi}, n_{\overline{1}}^{c,\theta}) = \mathbf{n}_{12} = (-\sin\frac{\Delta\theta}{2}, -\cos\frac{\Delta\theta}{2}),\\
& (n_{\underline{3}}^{c,\xi}, n_{\underline{3}}^{c,\theta}) = (n_{\overline{2}}^{c,\xi}, n_{\overline{2}}^{c,\theta}) = \mathbf{n}_{23} = (1, 0),\\
& (n_{\underline{4}}^{c,\xi}, n_{\underline{4}}^{c,\theta}) = (n_{\overline{3}}^{c,\xi}, n_{\overline{3}}^{c,\theta}) = \mathbf{n}_{34} = (-\sin\frac{\Delta\theta}{2}, \cos\frac{\Delta\theta}{2}),\\
& r_{\underline{1}}^c + r_{\overline{4}}^c = 2\xi_1 \sin\theta_c \cos\frac{\Delta\theta}{2}, \quad r_{\overline{2}}^c + r_{\underline{3}}^c = 2\xi_2 \sin\theta_c \cos\frac{\Delta\theta}{2},\\
& r_{\overline{1}}^c = (\frac{2}{3}\xi_1 + \frac{1}{3}\xi_2)\sin(\theta_c - \frac{\Delta\theta}{2}), \quad r_{\underline{2}}^c = (\frac{1}{3}\xi_1 + \frac{2}{3}\xi_2)\sin(\theta_c - \frac{\Delta\theta}{2}),\\
& r_{\overline{3}}^c = (\frac{1}{3}\xi_1 + \frac{2}{3}\xi_2)\sin(\theta_c + \frac{\Delta\theta}{2}), \quad r_{\underline{4}}^c = (\frac{2}{3}\xi_1 + \frac{1}{3}\xi_2)\sin(\theta_c + \frac{\Delta\theta}{2}),\\
& A_c = \frac{1}{2}(\xi_1 + \xi_2) l_3 \sin\Delta\theta.
\end{aligned} \tag{3.12}
$$

Substituting (3.9)-(3.12) into (3.4), we get

$$
\begin{aligned}
& m_c \frac{\mathrm{d}}{\mathrm{d}t}\begin{pmatrix} 1/\overline{\rho}_c \\ \overline{u}_c^{\xi} \\ \overline{u}_c^{\theta} \\ \overline{E}_c \end{pmatrix} \\
&= \begin{pmatrix} \sin\theta_c \cos\frac{\Delta\theta}{2}(\xi_2 l_2 u_4^c - \xi_1 l_1 u_1^c) \\ \sin\theta_c\{\frac{1}{6}[(2\xi_1+\xi_2)P_2^c + (\xi_1+2\xi_2)P_3^c] l_3 \sin\Delta\theta + (\xi_1 l_1 P_1^c - \xi_2 l_2 P_4^c)\cos\frac{\Delta\theta}{2}\} + A_c P_s \sin\theta_c \\ -\frac{1}{6}[(2\xi_1+\xi_2)P_2^c + (\xi_1+2\xi_2)P_3^c] l_3 \sin\Delta\theta\cos\theta_c + A_c P_s \cos\theta_c \\ \sin\theta_c \cos\frac{\Delta\theta}{2}(\xi_1 l_1 u_1^c P_1^c - \xi_2 l_2 u_4^c P_4^c) \end{pmatrix} \\
&= \begin{pmatrix} \sin\theta_c \cos\frac{\Delta\theta}{2}(\xi_2 l_2 u_4^c - \xi_1 l_1 u_1^c) \\ \sin\theta_c[\cos\frac{\Delta\theta}{2}(\xi_1 l_1 P_1^c - \xi_2 l_2 P_4^c) + 2A_c P_s] \\ -A_c P_s \cos\theta_c + A_c P_s \cos\theta_c \\ \sin\theta_c \cos\frac{\Delta\theta}{2}(\xi_1 l_1 u_1^c P_1^c - \xi_2 l_2 u_4^c P_4^c) \end{pmatrix} \\
&= \sin\theta_c \begin{pmatrix} \cos\frac{\Delta\theta}{2}(\xi_2 l_2 u_4^c - \xi_1 l_1 u_1^c) \\ \cos\frac{\Delta\theta}{2}(\xi_1 l_1 P_1^c - \xi_2 l_2 P_4^c) + 2A_c P_s \\ 0 \\ \cos\frac{\Delta\theta}{2}(\xi_1 l_1 u_1^c P_1^c - \xi_2 l_2 u_4^c P_4^c) \end{pmatrix}. \qquad (3.13)
\end{aligned}
$$

Since the cell is an equal-sided trapezoid, we have

$$m_c = \overline{\rho}_c V_c = \overline{\rho}_c r_c A_c = \overline{\rho}_c \xi_c A_c \sin\theta_c, \qquad (3.14)$$

where r_c and ξ_c are the values of r and ξ at the cell center respectively.

Thus from (3.13) and (3.14), we have

$$\frac{\mathrm{d}}{\mathrm{d}t}\begin{pmatrix} 1/\overline{\rho}_c \\ \overline{u}_c^{\xi} \\ \overline{u}_c^{\theta} \\ \overline{E}_c \end{pmatrix} = \frac{1}{\overline{\rho}_c \xi_c A_c} \begin{pmatrix} \cos\frac{\Delta\theta}{2}(\xi_2 l_2 u_4^c - \xi_1 l_1 u_1^c) \\ \cos\frac{\Delta\theta}{2}(\xi_1 l_1 P_1^c - \xi_2 l_2 P_4^c) + 2A_c P_s \\ 0 \\ \cos\frac{\Delta\theta}{2}(\xi_1 l_1 u_1^c P_1^c - \xi_2 l_2 u_4^c P_4^c) \end{pmatrix}. \qquad (3.15)$$

Finally we obtain the scheme (3.4) in the following detailed expression

$$\begin{pmatrix} 1/\overline{\rho}_c^{n+1} \\ \overline{u}_c^{\xi,n+1} \\ \overline{u}_c^{\theta,n+1} \\ \overline{E}_c^{n+1} \end{pmatrix} = \begin{pmatrix} 1/\overline{\rho}_c \\ \overline{u}_c^{\xi} \\ 0 \\ \overline{E}_c \end{pmatrix} + \frac{\Delta t}{\overline{\rho}_c \xi_c A_c} \begin{pmatrix} \cos\frac{\Delta\theta}{2}(\xi_2 l_2 u_4^c - \xi_1 l_1 u_1^c) \\ \cos\frac{\Delta\theta}{2}(\xi_1 l_1 P_1^c - \xi_2 l_2 P_4^c) + 2A_c P_s \\ 0 \\ \cos\frac{\Delta\theta}{2}(\xi_1 l_1 u_1^c P_1^c - \xi_2 l_2 u_4^c P_4^c) \end{pmatrix}. \qquad (3.16)$$

From the formula (3.16), we can see, at the $(n+1)$-th time step, the θ component of the cell velocity $\overline{\mathbf{u}}_c$ is zero and the magnitude of all the other conserved variables only depend on the radial position of the cell. The proof of the symmetry preservation property of the scheme is thus completed.

4 Numerical results in the two-dimensional cylindrical coordinates

In this section, we perform numerical experiments in two-dimensional cylindrical coordinates. Purely Lagrangian computation, the ideal gas with $\gamma = 5/3$, the initially equal-angled polar grid and the scheme (2.22)-(2.23) are used in the following tests unless otherwise stated. All the examples are performed by the scheme with local characteristic decomposition in the WENO reconstruction. Reflective boundary conditions are applied to the z and r axes in all the tests. u_ξ and u_θ represent the values of velocity in the radial and angular directions in the cell's local polar coordinates. The numerical results of the first order scheme shown in the following non-oscillatory tests for the purpose of comparison are obtained by the symmetry-preserving Lagrangian scheme developed in [8]. All the cells will be plotted in the following figures of density versus radial radius.

4.1 Accuracy test

We test the accuracy of the scheme (2.22)-(2.23) on a free expansion problem given in [21, 7]. The initial computational domain is $[0,1]\times[0,\pi/2]$ defined in the polar coordinates. At $t = 0$, we have

$$\rho = 1, \quad u_\xi = 0, \quad u_\theta = 0, \quad p = 1 - \xi^2,$$

where $\xi = \sqrt{z^2 + r^2}$.

The problem has the following analytical solution,

$$\begin{aligned}
&R(t) = \sqrt{1 + 2t^2},\\
&u_\xi(z,r,t) = \frac{2t}{1+2t^2}\xi, \quad u_\theta(z,r,t) = 0,\\
&\rho(z,r,t) = \frac{1}{R^3},\\
&p(z,r,t) = \frac{1}{R^5}\left(1 - \frac{\xi^2}{R^2}\right),
\end{aligned}$$

where R is the radius of the free outer boundary.

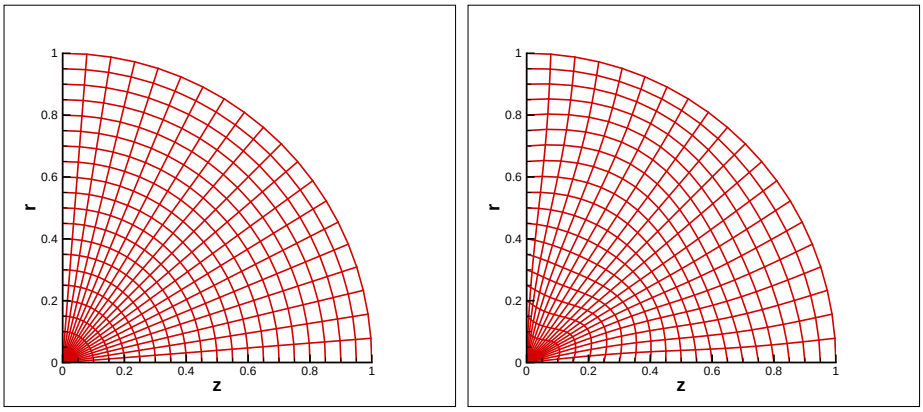

Figure 4.1: The initial grid of the free expansion problem with 20×20 cells. Left: equal-angled polar grid; Right: non-uniform smooth polar grid.

We perform the test on two different types of grids as shown in Figure 4.1. The first is an initially equal-angled polar grid. The second is an initially non-uniform smooth polar grid, for which each internal grid vertex is obtained by a smooth perturbation from an equal-angled polar grid as follows

$$z_{k,l} = \xi_k \cos\left(\frac{1}{2}\pi\theta_l\right) + \epsilon \sin(2\pi\xi_k)\sin(2\pi\theta_l),$$
$$r_{k,l} = \xi_k \sin\left(\frac{1}{2}\pi\theta_l\right) + \epsilon \sin(2\pi\xi_k)\sin(2\pi\theta_l),$$

where $\xi_k = \frac{k-1}{K-1}$, $\theta_l = \frac{l-1}{L-1}$, $(z_{k,l}, r_{k,l})$ is the z-r coordinate of the grid points with the sequential indices $(k,l), k = 1, ..., K-1, l = 2, ..., L-1$ in the radial and angular directions respectively. K, L represent the number of grid points in the above mentioned two directions. ϵ is a parameter which is chosen as 0.02 in this test.

Free boundary condition is applied on the outer boundary. Figure 4.2 shows the final grids. We can clearly observe symmetry in the left figure for the first type of grids. The errors of the scheme on these two kinds of grids at $t = 1$ are listed in Tables 4.1-4.2 which are measured on the interval $[\frac{1}{10}K, \frac{9}{10}K] \times [\frac{1}{10}L, \frac{9}{10}L]$ to remove the influence from the boundary. From both of these tables, we can see the expected second order accuracy at least in L_1-norm for all the evolved conserved variables.

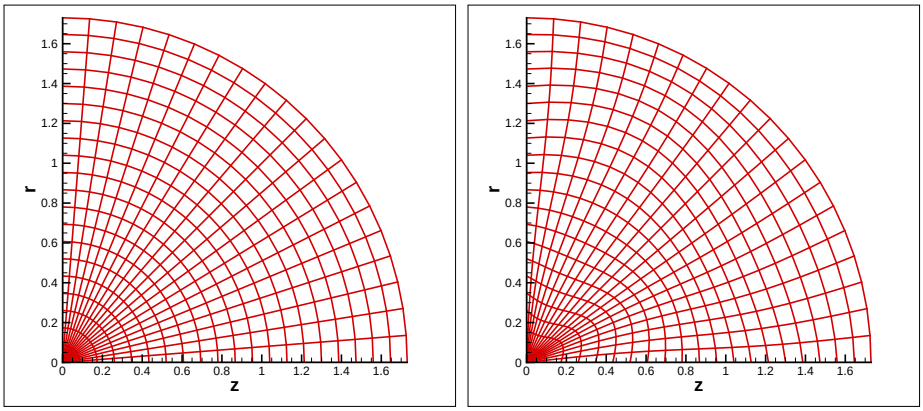

Figure 4.2: The final grid of the free expansion problem with 20×20 cells at $t = 1$. Left: initially equal-angled polar grid; Right: initially non-uniform smooth polar grid.

Table 4.1: Errors of the scheme in 2D cylindrical coordinates for the free expansion problem using $K \times L$ initially equal-angled polar grid cells

$K = L$	Norm	Density	order	Momentum	order	Energy	order
10	L_1	0.22E-2		0.18E-2		0.15E-2	
	L_∞	0.36E-2		0.41E-2		0.28E-2	
20	L_1	0.34E-3	2.69	0.22E-3	3.05	0.23E-3	2.71
	L_∞	0.59E-3	2.59	0.43E-3	3.27	0.45E-3	2.65
40	L_1	0.71E-4	2.25	0.39E-4	2.48	0.48E-4	2.30
	L_∞	0.15E-3	1.96	0.67E-4	2.66	0.11E-3	1.99
80	L_1	0.16E-4	2.18	0.80E-5	2.29	0.10E-4	2.20
	L_∞	0.41E-4	1.90	0.13E-4	2.34	0.28E-4	2.04

Table 4.2: Errors of the scheme in 2D cylindrical coordinates for the free expansion problem using $K \times L$ initially non-uniform smooth polar grid cells

$K = L$	Norm	Density	order	Momentum	order	Energy	order
10	L_1	0.22E-2		0.18E-2		0.15E-2	
	L_∞	0.38E-2		0.40E-2		0.30E-2	
20	L_1	0.34E-3	2.67	0.23E-3	2.99	0.24E-3	2.68
	L_∞	0.59E-3	2.68	0.36E-3	3.46	0.47E-3	2.67
40	L_1	0.72E-4	2.24	0.42E-4	2.45	0.49E-4	2.29
	L_∞	0.17E-3	1.81	0.50E-4	2.87	0.12E-3	2.00
80	L_1	0.16E-4	2.14	0.87E-5	2.28	0.11E-4	2.21
	L_∞	0.47E-4	1.85	0.12E-4	2.08	0.29E-4	2.03

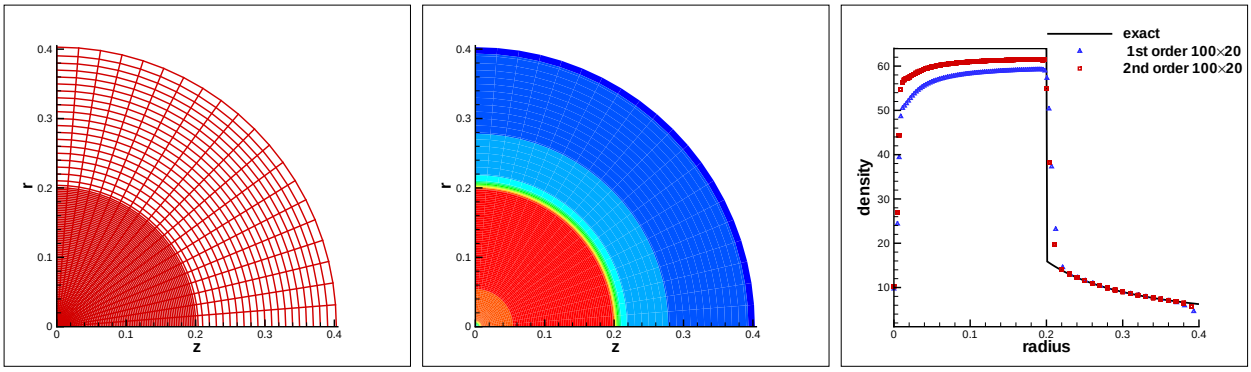

Figure 4.3: The results of the Noh problem with 100×20 cells at $t = 0.6$. Left: grid of the second order scheme; Middle: density contour of the second order scheme; Right: density versus radial radius. Solid line: exact solution; Blue symbols: first order scheme; Red symbols: second order scheme.

4.2 Non-oscillatory tests

Example 1 (The Noh problem in a cylindrical coordinate system on the polar grid [18]).

The Noh problem is a well-known test problem which is widely used to validate the performance of Lagrangian schemes on strong discontinuities. In this test case, the perfect gas has the following initial condition,

$$\rho = 1, \quad u_\xi = 1, \quad u_\theta = 0, \quad e = 10^{-5}.$$

The equal-angled polar grid is applied in the $\frac{1}{4}$-circle computational domain defined in the polar coordinates by $[0, 1] \times [0, \pi/2]$. The shock is generated by bringing the cold gas to rest at the origin. The analytical post shock density is 64 and the shock speed is 1/3. Figure 4.3 shows the results of the second order scheme (2.22)-(2.23) including the final grid and density contour with 100×20 cells at $t = 0.6$. The comparison of density as a function of the radial radius between the first order and second order schemes is also given on the right of Figure 4.3. From Figure 4.3, we observe the results are symmetric and non-oscillatory. The numerical solution is closer to the analytical solution with the usage of the second order scheme.

Example 2 (The spherical Sedov problem in a cylindrical coordinate system on the polar grid [21]).

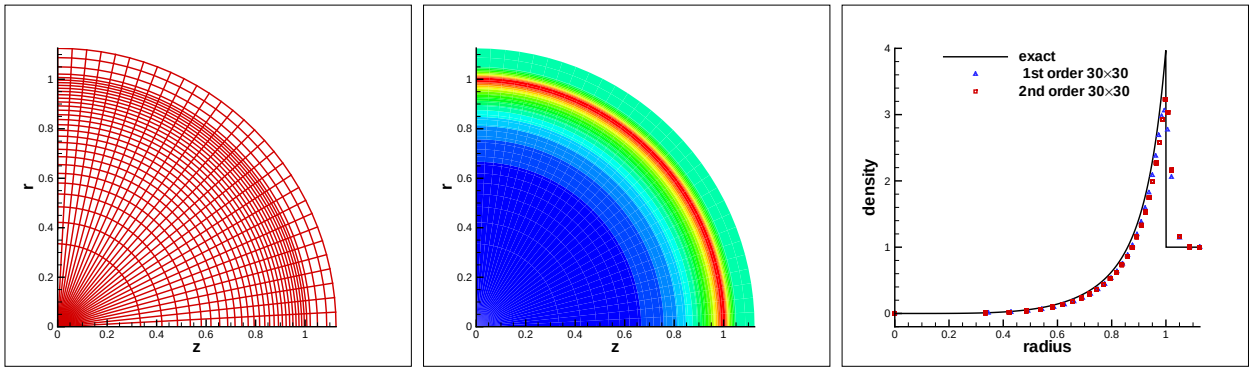

Figure 4.4: The results of the Sedov problem with 30×30 cells at $t = 1$. Left: grid of the second order scheme; Middle: density contour of the second order scheme; Right: density versus radial radius. Solid line: exact solution; Blue symbols: first order scheme; Red symbols: second order scheme.

The spherical Sedov blast wave problem in a cylindrical coordinate system is a commonly used example of a diverging shock wave. The initial computational domain is a $\frac{1}{4}$-circle region defined in the polar coordinates by $[0, 1.125] \times [0, \pi/2]$. The initial condition is,

$$\rho = 1, \quad u_\xi = 0, \quad u_\theta = 0,$$

the specific internal energy e is zero except in the cells connected to the origin where they share a total value of 0.2468. Reflective boundary condition is applied on the outer boundary. The analytical solution is a shock with a peak density of 4 at radius unity at time unity. The final grid and the surface of density obtained by the second order scheme (2.22)-(2.23) with 30×30 cells are displayed in Figure 4.4. The comparison of density as a function of the radial radius between the first order and second order schemes is shown on the right of Figure 4.4. We observe the expected symmetry in the plots of grid and density. The shock position and peak density obtained by the second order scheme coincide with the analytical solutions better than those obtained by the first order scheme, which demonstrates the good performance of the second order scheme in symmetry preserving, non-oscillation and accuracy properties.

Example 3 (The one-dimensional spherical Sod Riemann problem).

For this problem, the initial computational domain is $[0, 20] \times [0, \pi/2]$ defined in the polar

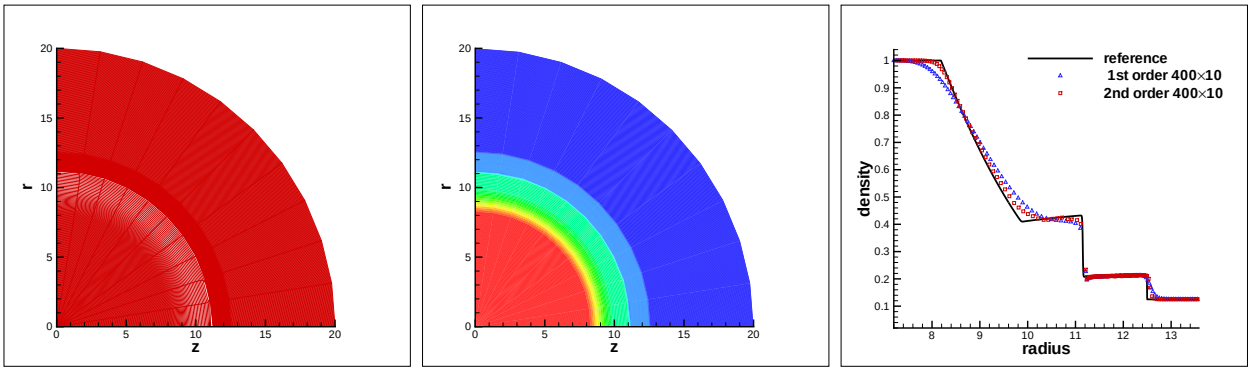

Figure 4.5: The results of the Sod problem with 400×10 cells at $t = 1.4$. Left: grid of the second order scheme; Middle: density contour of the second order scheme; Right: density versus radial radius. Solid line: exact solution; Blue symbols: first order scheme; Red symbols: second order scheme.

coordinates. Its initial condition is as follows

$$(\rho, u_\xi, u_\theta, p) = \begin{cases} (1, 0, 0, 1), & 0 \le \xi \le 10 \\ (0.125, 0, 0, 0.1), & 10 < \xi \le 20 \end{cases}$$

The reflective boundary condition is applied on the outer boundary. The grid consists of 400×10 equal-angled polar cells. The reference solution is the converged result obtained by using a one-dimensional second-order Eulerian code in the spherical coordinate with 10000 grid points. Figure 4.5 shows the numerical results of the grid and density contour of the second order scheme, and density as a function of the radial radius performed by both the second order scheme and the first order scheme at $t = 1.4$. We observe the good symmetry behavior of the schemes and the better agreement between the numerical result of the second order scheme and the reference solution.

Example 4 (Kidder's isentropic compression problem [11, 15]).

This problem is a self-similar problem with a spherical isentropic compression. At the initial time, the shell has a ring shape with the computational region $[0.9, 1] \times [0, \pi/2]$ in the polar coordinates. $u_\xi = 0, u_\theta = 0$. The initial density and pressure ρ_0, P_0 have the following expression,

$$\rho_0(\xi) = \left(\frac{\xi_4 - \xi^2}{\xi_4 - \xi_3} \rho_1^{\gamma-1} + \frac{\xi^2 - \xi_3}{\xi_4 - \xi_3} \rho_2^{\gamma-1} \right)^{\frac{1}{\gamma-1}}, \quad P_0(\xi) = s(\rho_0(\xi))^\gamma,$$

where $\rho_1 = 6.31 \times 10^{-4}$, $\rho_2 = 10^{-2}$, $s = 2.15 \times 10^4$, $\gamma = 5/3$. With the time marching, the pressure $P_1(t)$ and $P_2(t)$ are imposed continuously at the internal and external boundary respectively which have the following representation

$$P_1(t) = P_1^0 a(t)^{-\frac{2\gamma}{\gamma-1}}, \quad P_2(t) = P_2^0 a(t)^{-\frac{2\gamma}{\gamma-1}}$$

where $P_1^0 = 0.1$, $P_2^0 = 10$ and $a(t) = \sqrt{1-(\frac{t}{\tau})^2}$ in which $\tau = 6.72 \times 10^{-3}$ is the focusing time of the shell and $t \in [0, \tau)$ is the evolving time.

The analytical solutions of the three fundamental variables for this problem in spherical geometry are as follows

$$\begin{aligned}
\rho(\zeta(\xi,t),t) &= \rho_0(\xi)\xi a(t)^{-\frac{2}{\gamma-1}}, \\
u(\zeta(\xi,t),t) &= \xi \frac{\mathrm{d}}{\mathrm{d}t} a(t), \\
p(\zeta(\xi,t),t) &= P_0(\xi)\xi a(t)^{-\frac{2\gamma}{\gamma-1}},
\end{aligned}$$

where $\zeta(\xi,t)$ is denoted to be the radius at time t of a point initially located at radius ξ, its analytical solution is $\zeta(\xi,t) = a(t)\xi$.

We test the second order scheme (2.22)-(2.23) on this problem with initially 80×40 equal-angular cells. The final time is set to be $t = 0.99\tau$. Figure 4.6 shows the final grid and density contour, from which we observe perfect symmetry. Figure 4.7 shows the results of density, velocity and pressure obtained by both the second order scheme and the first order scheme at the final time where we can observe the numerical solutions obtained by the second order scheme are much closer to the analytical solutions.

Example 5 (Implosion problem of Lazarus [12]).

In this self-similar implosion problem, initially a sphere of unit radius has the following condition,

$$\rho = 1, \quad u_\xi(t) = \frac{-\alpha f}{(1-ft)^{1-\alpha}}, \quad u_\theta(t) = 0, \quad e = 10^{-5}, \tag{4.1}$$

where $\alpha = 0.6883545$, $f = 1 - \varepsilon t - \delta t^3$, $\varepsilon = 0.185$, $\delta = 0.28$.

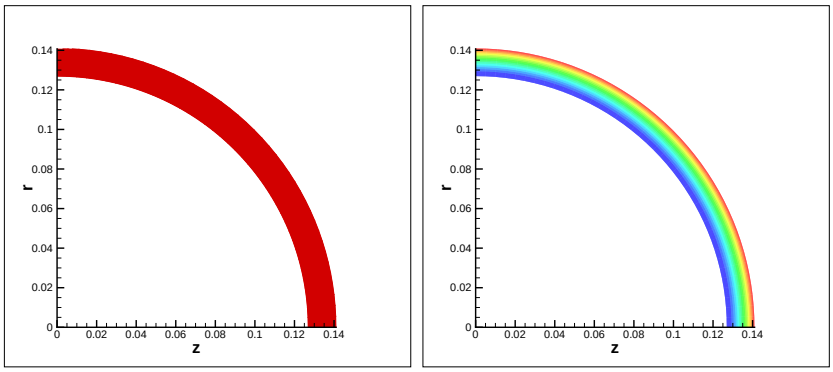

Figure 4.6: The results of the Kidder problem with 80×40 cells at $t = 0.99\tau$. Left: grid of the second order scheme; Right: density contour of the second order scheme.

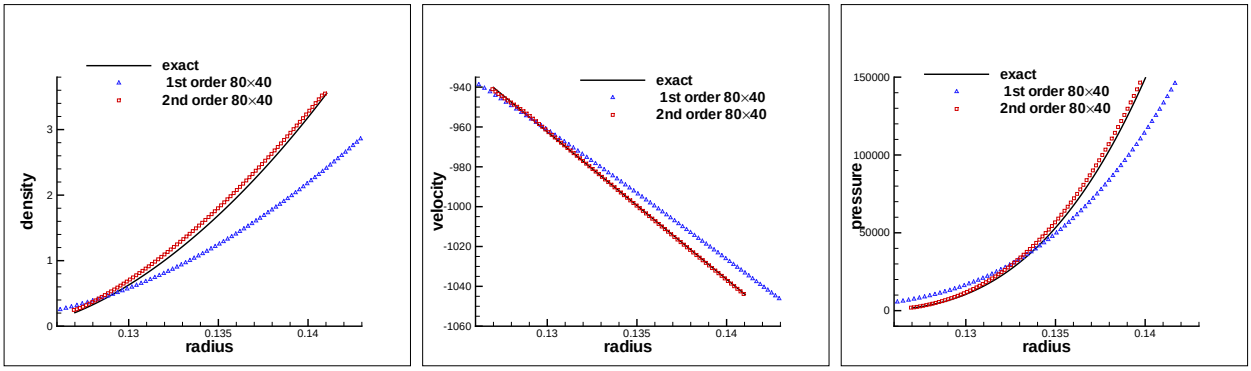

Figure 4.7: The results of the Kidder problem at $t = 0.99\tau$ with 80×40 cells. Left: density vs radial radius; Middle: velocity vs radial radius; Right: pressure vs radial radius. Solid line: exact solution; Blue symbols: first order scheme; Red symbols: second order scheme.

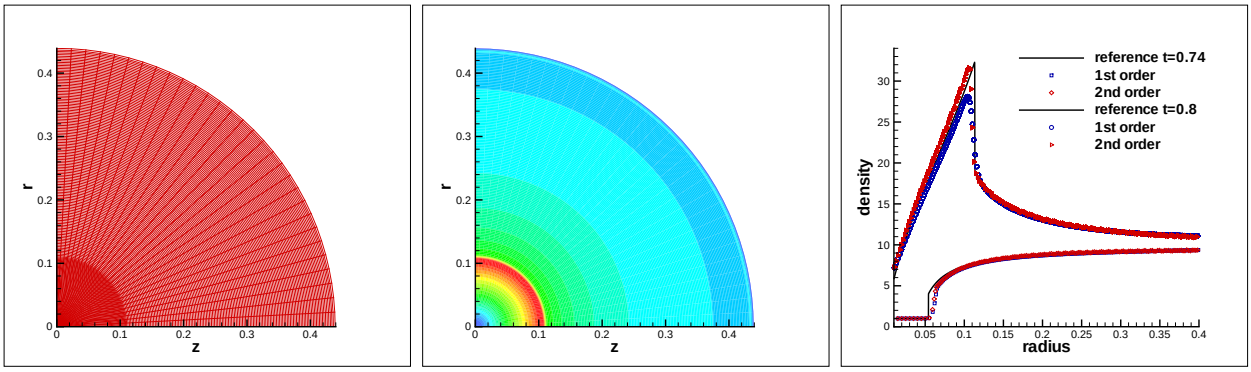

Figure 4.8: The results of the Lazarus problem with 200×30 cells. Left: grid of the second order scheme at $t = 0.8$; Middle: density contour of the second order scheme at $t = 0.8$; Right: density vs radial radius at $t = 0.74$, 0.8. Solid line: reference solution; Blue symbols: first order scheme; Red symbols: second order scheme.

We test the problem on a grid of 200×30 cells in the initial computational domain $[0, 1] \times [0, \pi/2]$ defined in the polar coordinates. The numerically converged result computed using a one-dimensional second-order Lagrangian code in the spherical coordinate with 10000 cells is used as a reference solution. We display the results of the second order scheme (2.22)-(2.23) in Figure 4.8. In the plots of grid and density contour, we notice the expected symmetry. In the plot of density as a function of the radial radius, we observe the non-oscillatory property of the scheme. By comparing with the first order scheme, we observe that the second order scheme produces more accurate numerical solution.

Example 6 (Coggeshall expansion problem [9]).

In this example, we attempt to apply a two-dimensional adiabatic compression problem proposed by Coggeshall to test the performance of the second order scheme (2.22)-(2.23) on a truly two-dimensional problem. The computational domain is $[0, 1] \times [0, \pi/2]$ defined in the polar coordinates with 100×10 equal-angular cells. The initial condition is as follows,

$$\rho = 1, \quad (u_z, u_r) = (-z/4, -r), \quad e = (3z_c/8)^2,$$

where z_c is the z coordinate of the cell center. Figure 4.9 shows the results of the grid, density contour and density plotted as a function of the radial radius along each radial line at $t = 0.8$ in which time the analytical density is expected to be flat with a value of 37.4.

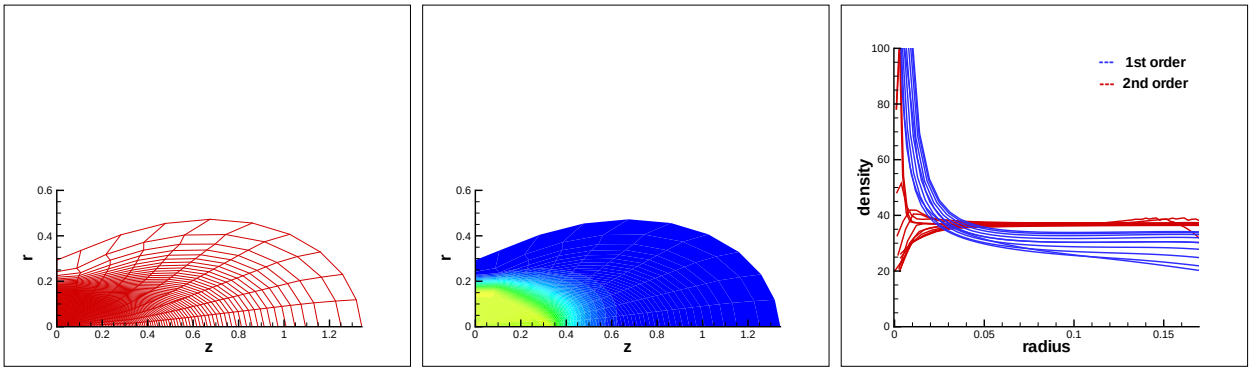

Figure 4.9: The results of the Coggeshall problem with 100×10 cells at $t = 0.8$. Left: grid of the second order scheme; Middle: density contour of the second order scheme; Right: density versus radial radius. Blue symbols: first order scheme; Red symbols: second order scheme.

From the figures, we can observe the numerical results performed by the second order scheme agree with the analytical solution much better except for the small region near the origin.

Example 7 (Spherical Sedov problem on the Cartesian grid).

The spherical symmetry problem simulated on the initially rectangular grid is demonstrated to be much more challenging for a Lagrangian scheme due to the shock direction being not aligned with the grid line. In this example, we test the spherical Sedov blast wave problem in a cylindrical coordinate system on the initially rectangular grid. The initial computational domain is a 1.125×1.125 square consisting of 50×50 uniform cells. Its initial condition is

$$\rho = 1, \quad u_z = 0, \quad u_r = 0.$$

The specific internal energy e is zero except in the cell connected to the origin where it has a value of 0.2468. Figure 4.10 shows the results of our second order scheme (2.22)-(2.23) and the first order scheme. From the figures, we can observe the results of our second order scheme are symmetric and more accurate than the first order scheme even on this non-polar grid.

Example 8 (Spherical Noh problem on the Cartesian grid [18]).

In this example, we test the spherical Noh implosion problem on a Cartesian grid to verify

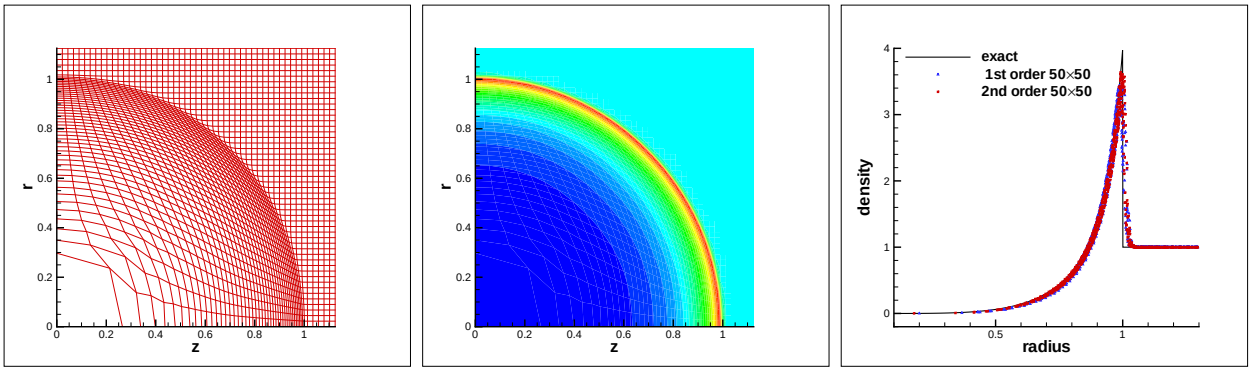

Figure 4.10: The results of the Sedov problem with 50×50 Cartesian cells at $t = 1.0$. Left: grid of the second order scheme; Middle: density contour of the second order scheme; Right: density versus radial radius. Solid line: exact solution; Blue symbols: first order scheme; Red symbols: second order scheme.

the robustness of the scheme. This problem is a very severe test for a Lagrangian scheme computed on a Cartesian grid, since in this case the grid near the axes is easy to be distorted which has been addressed in [5]. The initial domain is $[0, 1] \times [0, 1]$. The initial state of the fluid is $(\rho, u_\xi, u_\theta, e) = (1, -1, 0, 10^{-5})$, where u_ξ, u_θ are the radial and angular velocities at the cell center. Reflective boundary conditions are applied on the left and bottom boundaries. Free boundary condition is used on the right and top boundaries. The analytical solution is the same as that in Example 1. Figure 4.11 shows the result of the second order scheme (2.22)-(2.23) with 60×60 initially uniform rectangular cells at $t = 0.6$. From these figures, we can see that there is no grid distortion along the axes, the spherical symmetry of the shock front is preserved well and the shock position is correct, which demonstrate the robustness of the scheme on the Cartesian grid.

Example 9 (Implosion problem of Lazarus simulated on the semi-circle domain [12, 13]).

To demonstrate the robustness of our scheme, we further perform the test on the previously mentioned Lazarus problem with a grid of 50×50 cells on an initially semi-circle domain of unit initial radius with a center of convergence at $(z, r) = (0, 0)$ and a center of convergence at $(z, r) = (0.5, 0)$ respectively, see the left figures in Figures 4.12-4.13 for the initial grids. In both cases the velocity boundary condition is the same as that in Example 5, which is given by (4.1). We display the results of the second order scheme (2.22)-(2.23) in

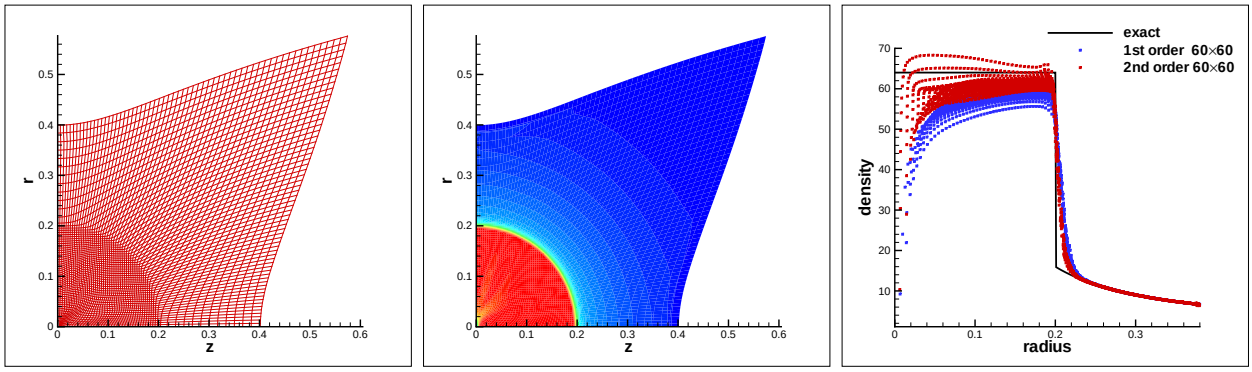

Figure 4.11: The results of the Noh problem with 60×60 Cartesian cells at $t = 0.6$. Left: grid of the second order scheme; Middle: density contour of the second order scheme; Right: density versus radial radius. Solid line: exact solution; Blue symbols: first order scheme; Red symbols: second order scheme.

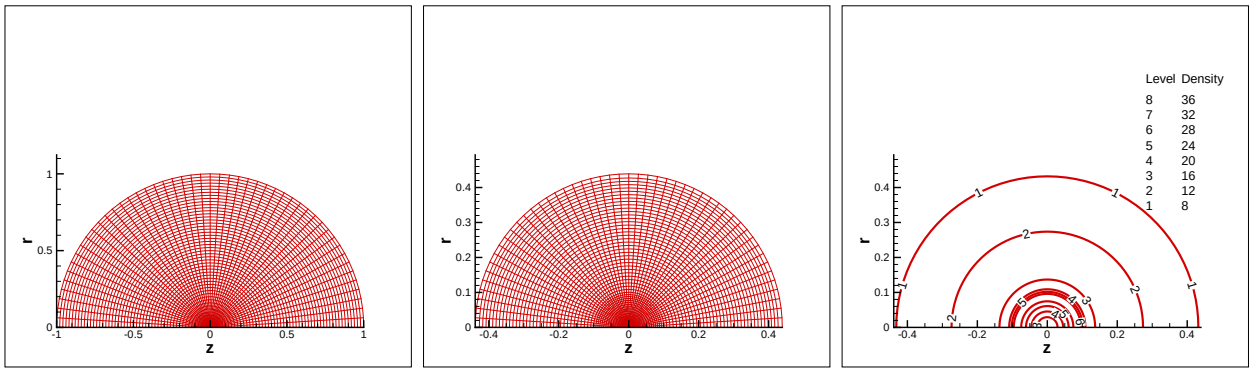

Figure 4.12: The results of the Lazarus problem on a semi-circle domain with a center of convergence at $(z, r) = (0, 0)$ initially. Left: the initial grid with 50×50 cells; Middle: grid of the second order scheme at $t = 0.8$; Right: density contour of the second order scheme at $t = 0.8$.

Figure 4.12 and Figure 4.13. In the plots of density contour at $t = 0.8$, we notice the results on these two types of grids are quite comparable, which shows the good performance of our scheme on robustness.

5 Concluding remarks

In this paper we develop a new second order cell-centered symmetry-preserving Lagrangian scheme for solving compressible Euler equations in the two-dimensional cylindrical coordinates. The scheme is based on the control volume discretizations. It is designed to have uniformly second order accuracy and to be able to preserve one-dimensional spherical sym-

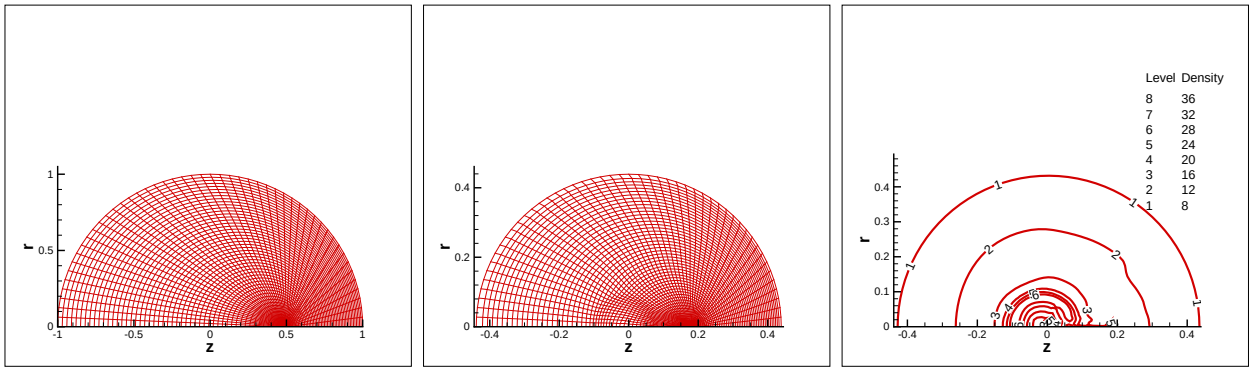

Figure 4.13: The results of the Lazarus problem on a semi-circle domain with a center of convergence at $(z, r) = (0.5, 0)$ initially. Left: the initial grid with 50×50 cells; Middle: grid of the second order scheme at $t = 0.8$; Right: density contour of the second order scheme at $t = 0.8$.

metry in a two-dimensional cylindrical geometry when computed on an equal-angle-zoned initial grid, and meanwhile it maintains many other good properties such as conservation for mass, momentum and total energy and the geometric conservation law. Several two-dimensional numerical examples in cylindrical coordinates are presented to demonstrate the good performance of the scheme in terms of accuracy, symmetry, non-oscillation and robustness properties. The improvement of the scheme on other important properties such as positivity-preserving constitutes our future work.

References

[1] A. Barlow, D. Burton and M. Shashkov, *Compatible, energy and symmetry preserving 2D Lagrangian hydrodynamics in rz - cylindrical coordinates*, Procedia Computer Science, 1, 2010, 1887-1895.

[2] D.J. Benson, *Computational methods in Lagrangian and Eulerian hydrocodes*, Computer Methods in Applied Mechanics and Engineering, 99, 1992, 235-394.

[3] P.L. Browne, *Integrated gradients: a derivation of some difference forms for the equation of motion for compressible flow in two-dimensional Lagrangian hydrodynamics, using*

integration of pressures over surfaces, Los Alamos National Laboratory Report LA-2105872-MS, 1986.

[4] E.J. Caramana, D.E. Burton, M.J. Shashkov and P.P. Whalen, *The construction of compatible hydrodynamics algorithms utilizing conservation of total energy*, Journal of Computational Physics, 146, 1998, 227-262.

[5] J.C. Campbell and M.J. Shashkov, *A tensor artificial viscosity using a mimetic finite difference algorithm*, Journal of Computational Physics, 172, 2001, 739-765.

[6] J. Cheng and C.-W. Shu, *A high order ENO conservative Lagrangian type scheme for the compressible Euler equations*, Journal of Computational Physics, 227, 2007, 1567-1596.

[7] J. Cheng and C.-W. Shu, *A cell-centered Lagrangian scheme with the preservation of symmetry and conservation properties for compressible fluid flows in two-dimensional cylindrical geometry*, Journal of Computational Physics, 229, 2010, 7191-7206.

[8] J. Cheng and C.-W. Shu, *Improvement on spherical symmetry in two-dimensional cylindrical coordinates for a class of control volume Lagrangian schemes*, Communications in Computational Physics, 11, 2012, 1144-1168.

[9] S.V. Coggeshall and J. Meyer-ter-Vehn, *Group invariant solutions and optimal systems for multidimensional hydrodynamics*, Journal of Mathematical Physics, 33, 1992, 3585-3601.

[10] G. Jiang and C.-W. Shu, *Efficient implementation of weighted ENO schemes*, Journal of Computational Physics, 126, 1996, 202-228.

[11] R.E. Kidder, *Laser-driven compression of hollow shells: power requirements and stability limitations*, Nuclear Fusion, 1, 1976, 3-14.

[12] R. Lazarus, *Self-similar solutions for converging shocks and collapsing cavities*, SIAM Journal on Numerical Analysis, 18, 1981, 316-371.

[13] R. Loubère and E.J. Caramana, *The force/work differencing of exceptional points in the discrete, compatible formulation of Lagrangian hydrodynamics*, Journal of Computational Physics, 216, 2006, 1-18.

[14] X.-D. Liu, S. Osher and T. Chan, *Weighted essentially non-oscillatory schemes*, Journal of Computational Physics, 115, 1994, 200-212.

[15] P.-H. Maire, *A high-order cell-centered Lagrangian scheme for compressible fluid flows in two-dimensional cylindrical geometry*, Journal of Computational Physics, 228, 2009, 6882-6915.

[16] P.-H. Maire, R. Loubère and Pavel Váchal, *Staggered Lagrangian discretization based on cell-centered Riemann solver and associated hydrodynamics scheme*, Communications in Computational Physics, 10, 2011, 940-978.

[17] L.G. Margolin and M.J. Shashkov, *Using a curvilinear grid to construct symmetry-preserving discretizations for Lagrangian gas dynamics*, Journal of Computational Physics, 149, 1999, 389-417.

[18] W.F. Noh, *Errors for calculations of strong shocks using an artificial viscosity and an artificial heat flux*, Journal of Computational Physics, 72, 1987, 78-120.

[19] P. Váchal and B. Wendroff, *A symmetry preserving dissipative artificial viscosity in an r-z staggered Lagrangian discretization*, Journal of Computational Physics, 258, 2014, 118-136.

[20] W.D. Schulz, *Two-dimensional Lagrangian hydrodynamic difference equations*, Methods of Computational Physics, 3, 1964, 1-45.

[21] L.I. Sedov, *Similarity and Dimensional Methods in Mechanics*, Academic Press, New York, 1959.

[22] C.-W. Shu and S. Osher, *Efficient implementation of essentially non-oscillatory shock-capturing schemes*, Journal of Computational Physics, 77, 1988, 439-471.

[23] C.-W. Shu, T.A. Zang, G. Erlebacher, D. Whitaker and S. Osher, *High-order ENO schemes applied to two- and three-dimensional compressible flow*, Applied Numerical Mathematics, 9, 1992, 45-71.

[24] A. Solov'ev and M. Shashkov, *Difference scheme for the Dirichlet particle method in cylindrical method in cylindrical coordinates, conserving symmetry of gas-dynamical flow*, Differential Equations, 24, 1988, 817-823.

[25] M.L. Wilkins, *Calculation of elastic plastic flow*, Methods of Computational Physics, 3, 1964, 211-263.